Journal of Computational Chemistry

WILEY

Journal of COMPUTATIONAL CHEMISTRY

RESEARCH ARTICLE OPEN ACCESS

Chemical Bond Overlap Descriptors From Multiconfiguration Wavefunctions

Carlos V. Santos-Jr[1] | Elfi Kraka[2] | Renaldo T. Moura Jr[2,3]

[1]Department of Chemistry, Federal University of Paraiba, João Pessoa, Brazil | [2]Department of Chemistry, Computational and Theoretical Chemistry Group (CATCO), Southern Methodist University, Dallas, Texas, USA | [3]Department of Chemistry and Physics, Center of Agrarian Sciences, Federal University of Paraiba, Areia, Brazil

Correspondence: Renaldo T. Moura Jr (renaldo.mourajr@cca.ufpb.br)

Received: 29 September 2024 | **Revised:** 4 November 2024 | **Accepted:** 7 November 2024

Funding: This work was supported by Brazilian National Council for Scientific and Technological Development—CNPq, Grant numbers 406483/2023-0, and 310988/2023-3; Public Call n. 03 Produtividade em Pesquisa PROPESQ/PRPG/UFPB project number PVN13305-2020 and CAPES Demanda Social 88887.659768/2021-00 and the National Science Foundation (NSF), Grant CHE 2102461.

Keywords: LVM | MCSCF | overlap model | QTAIM

ABSTRACT

The chemical bond is a fundamental concept in chemistry, and various models and descriptors have evolved since the advent of quantum mechanics. This study extends the overlap density and its topological descriptors (OP/TOP) to multiconfigurational wavefunctions. We discuss a comparative analysis of OP/TOP descriptors using CASSCF and DCD-CAS(2) wavefunctions for a diverse range of molecular systems, including X–O bonds in X–OH (X═H, Li, Na, H_2B, H_3C, H_2N, HO, F) and Li–X′ (X═F, Cl, and Br). Results show that OP/TOP aligns with bonding models like the quantum theory of atoms in molecules (QTAIM) and local vibrational modes theory, revealing insights such as overlap densities shifting towards the more electronegative atom in polar bonds. The Li–F dissociation profile using OP/TOP descriptors demonstrated sensitivity to ionic/neutral inversion during Li–F dissociation, highlighting their potential for elucidating complex bond phenomena and offering new avenues for understanding multiconfigurational chemical bond dynamics.

1 | Introduction

Chemical bonds represent a fundamental and pervasive concept in chemistry, providing an intrinsic foundation that assists chemists in comprehending the properties and characteristics of molecules and materials as well as their potential reactions. Since the inception of quantum mechanics [1–4], a multitude of theories have arisen to model and characterize the nature of chemical bonds, resulting in the development of diverse chemical bond descriptors from various perspectives [5, 6]. Some of the most renowned approaches for analyzing chemical bonds can be broadly categorized into three groups. The first group includes energy-based descriptors, such as the Bond Dissociation Energy (BDE) or Binding Energy (BE) [7] and related Energy Decomposition Analysis schemes (EDA) [8–12], or the Activation Strain Model (ASM) [13]. One has to keep in mind that energies and related properties only provide an overall insight into chemical bonding given their cumulative nature, that is, reflecting the energy needed for bond breaking, but also containing energy contributions due to geometry relaxation and electron density reorganization in the dissociation fragments [14–19]. The second group comprises methods based on wavefunction or electron density analysis, such as the Quantum Theory of Atoms in Molecules (QTAIM) [20–23], the Electron Localization Function (ELF) [24] and the Electron Localizability Indicator (ELI-D), as well as Molecular Orbital (MO) analysis [25] and Natural Bond Orbitals (NBO) analysis [26, 27]. A third group is based on vibrational spectroscopy with the Local Vibrational Mode (LVM) theory [28–34] as the most prominent representative.

Recently a new set of density-based-decomposition bond descriptors was introduced as part of the Chemical Bond Overlap (OP) model [35]. The OP model builds upon overlap properties initially introduced by Malta, Batista, and Carlos [36], encompassing a range of chemical bond descriptors that have been expanded in recent work [37]. This extension includes topological descriptors (TOP) derived from a numerically obtained overlap density through localized molecular orbitals. Originally devised for the analysis of diatomic or diatomic-like systems [36], the OP model initially found utility in describing Ln–L bonds within lanthanide complexes [38]. Subsequently, it has proven versatile and has been successfully applied to a variety of systems, including diatomics [39, 40], molecular species [35, 41], coordination compounds [42–45], and solid-state materials [40, 46]. An understanding of overlap polarizability is crucial for comprehending the relationship between 4f–4f transition intensities and the covalent character of Ln–L bonds [30, 44, 47, 48]. Moreover, the OP approach has been effectively employed to describe chemical bonding in organic reaction systems [41]. This application has yielded results in excellent agreement with other chemical bond analysis models, such as Quantum Theory of Atoms in Molecules (QTAIM) [20] and Local Vibrational Mode (LVM) [28, 29, 31].

All of the previously mentioned methods (BDE, EDA, ASM, LVM, QTAIM, ELF, and NBO) provide chemical bond descriptors that are only as accurate as the model chemistry employed to describe the wavefunction and/or the electron density of the target molecular system. In this context, the simplicity and computational efficiency of Density Functional Theory (DFT) methods and approximations, which implicitly handle electron correlation, may falter when dealing with strong correlation effects, that is, systems with significant multireference character [49].

Wavefunction theory has long established that not all chemical species can be adequately represented by a single-determinant wavefunction. For cases where the electronic state of a molecule cannot be reasonably described by a single Slater determinant, the Complete Active Space Self-Consistent Field (CASSCF) method [50] provides a robust approach to account for static electron correlation. To further address dynamic electron correlation, widely used post-CASSCF methods include Complete Active Space Second-Order Perturbation Theory (CASPT2) [51, 52] and Second-Order N-Electron Valence State Perturbation Theory (NEVPT2) [53].

Many studies have emphasized the necessity of multiconfigurational approaches for achieving more accurate descriptions of a wide range of molecules. Kraka, He, and Cremer [54] pointed out that when a molecule contains multiple bonded electronegative atoms, a high degree of multiconfigurational character is often expected. They explored how different levels of theory describe the equilibrium geometry of the FOOF molecule, noting that while MP6/CBS provided the most reasonable estimate among single-determinant methods, multiconfigurational approaches could offer a more realistic description. Similarly, Wardzala et al. [55] emphasized the importance of multiconfigurational methods in understanding chemical reactivity, especially in transition states and intermediates. Wysocki and Park [56] reported the implementation and application of Douglas-Kroll-Hess (DKH2) CASSCF calculations to determine the magnetic properties of atoms, diatomic molecules containing d-metal atoms, and large Tb-based systems within the Molcas/OpenMolcas program. Loreti et al. [57] introduced the wave function overlap tool (WFOT), designed to evaluate the overlap between wave functions computed at both single-reference and multireference levels of electronic structure theory. Verma and Truhlar [58] provided a comprehensive assessment of the accuracy of DFT in predicting charge distributions for single-reference and multireference molecules, concluding that, as expected, single-reference DFT performs less effectively for multireference systems. Recently, Carlson, Truhlar, and Gagliardi [59, 60] introduced multiconfiguration pair-density functional theory (MC-PDFT), which offers improved accuracy for systems with significant multireference character, including molecules containing transition metals. Grimme and Waletzke [61] proposed computational strategies and algorithms to perform multi-reference Møller-Plesset (MR-MP2) calculations efficiently for large molecules, achieving accuracy comparable to CASPT2 but with reduced computational costs.

Given that CASPT2 and NEVPT2 methods retain a frozen 0th-order wavefunction [62], any chemical bond descriptor being, for example, based on the electron density derived from this 0th-order wavefunction reflects the quality of the pure CASSCF ansatz, that is, the descriptor does not account for dynamic correlation. This scenario is commonly found in numerous applications of QTAIM across various systems, a few of which are highlighted below.

Malček et al. [63] explored how QTAIM describes electronic densities in M–M bonds (M═Cu, Cr) within tetrakis complexes, considering both single-determinant methods and CASSCF. Additionally, Li et al. [64] provided QTAIM descriptors for M–M (M═B, Al, and Ga) bonds in M_3 clusters, utilizing the CASSCF wavefunction. Their findings revealed the presence of 3-center-2-electron bonds and classified B–B and Al–Al bonds as covalent, while Ga–Ga bonds exhibited metallic behavior. Giricheva et al. [65] investigated the nature of the Co–O bond in Gaseous Oxopivalate Cobalt(II) using QTAIM topological descriptors with the CASSCF wavefunction. Pech et al. [66] conducted an investigation into the effects of spin-orbital coupling in astatine diatomic molecules and trihalide anions. Their study revealed that spin-orbital coupling reduces the covalent nature of At–X bonds, where X represents At, I, Br, Cl, or F. Reuter and Lüchow [67] introduced a QTAIM-based methodology for predicting the composition of ionic or covalent bonds, employing Valence Bond or CASSCF wave functions. Their study demonstrates the effectiveness of this model on small, well-known molecules. Zhabanov and Zhabanov [68] employed QTAIM to analyze CASSCF wavefunctions in order to investigate chemical bonds in iron and cobalt metal complexes of porphyrazines.

In contrast to density-based descriptors, CASPT2 and NEVPT2 energy-based descriptors, including descriptors based on first, and second energy derivatives, incorporate dynamics correlation effects, making them superior. However, as mentioned above, these descriptors provide only an overall measure of bond strength, caused by their cumulative nature. It is critical to acknowledge that dynamic correlation effects may exert a significant influence on certain chemical systems. For systems exhibiting both pronounced static and dynamic correlation

effects, Multi-Reference (MR) Configuration Interaction (CI) methods are particularly suitable. These methods handle multireference situations where single-reference approaches might be inadequate. However, it is important to consider that the computational costs associated with MRCI methods can be substantial, particularly for larger systems. High-level multireference (MR) methods, such as configuration interaction with single and double excitations (MR-CISD) and averaged quadratic coupled-cluster (MR-AQCC), along with their variants, are a specialty of the COLUMBUS software [69, 70], which employs the graphical unitary group approach (GUGA) [71, 72]. Hans Lischka has played a pivotal role in the development of new methodologies and tools for the application of Multiconfigurational Self-Consistent Field (MCSCF) and MRCI methods [73], contributing to various aspects of quantum chemistry calculations [73–77].

Despite ongoing efforts, MR-CISD and the aforementioned methodologies still present high computational costs and significant time demands. Pathak, Lang, and Neese [78] also provided a thoughtful discussion on incorporating dynamic correlation effects into the 0th-order wavefunction. Their work introduced the Dynamic Correlation Dressed Complete Active Space with Second-Order Treatment (DCD-CAS(2)) method. They highlighted the cost-effectiveness and superior performance of this approach when compared to NEVPT2 energies.

In light of the significance of MCSCF methods for providing a more accurate description of chemical bond descriptors for notorious multireference systems [70], this report elaborates on the extension of OP/TOP descriptors using MCSCF wavefunctions. Initially, we demonstrate that canonical molecular orbitals yield a consistent representation of the overlap density comparable to that obtained using their localized molecular orbitals counterparts. The implementation is designed to be applicable to any multideterminantal type of wavefunction, such as MCSCF, MR-CI, MR-CISD, MC-PDFT, or similar methods. In order to showcase this new functionality, we discuss in this paper a comparative analysis between OP/TOP descriptors using CASSCF wavefunctions as a representative example. Additionally, a complementary study focusing on the dissociation profile of the Li–F bond is presented, utilizing the DCD-CAS(2) wavefunction. The H_2O molecule **01** served as a benchmark example for the evaluation of basis set and active space size convergence, while the set of test examples **02**–**12**, presented in Figure 1, were adopted to challenge the MCSCF implementation of OP/TOP bond descriptors, reported in this work, and their comparison with QTAIM and LVM descriptors. The targeted bonds in polyatomic molecules were selected from the report by Fugel et al. [79]. The dissociation pattern of the Li–F bond was selected to emphasize the differences in OP/TOP descriptors when using the CASSCF and a second-order corrected wavefunction (DCD-CAS(2)).

2 | Methodology

We begin the methodology section by demonstrating that canonical molecular orbitals (MOs) provide a consistent representation of the overlap density comparable to that obtained using their localized molecular orbitals (LMOs) counterparts. Subsequently,

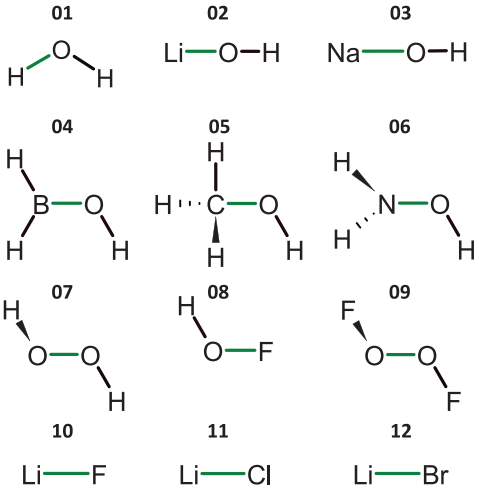

FIGURE 1 | Schematic representation of the studied molecular systems. The examined chemical bonds are highlighted in green.

we derive the overlap density from an MCSCF wavefunction. Finally, we will delve into the main OP/TOP descriptors.

2.1 | Electron Density Overlap Terms From Canonical and Localized MOs

Stewart [27] emphasized the importance of LMOs for theoretical chemistry. One of the most valuable advantages of using LMOs is the possibility to interpret chemical problems through concepts derived from a Lewis notation, allowing the association of LMOs with two-electron bonds, lone-pairs, and π delocalization.

The expanded OP model, introduced in 2020 [35] decomposes the electron density of a single LMO into atomic (one-center) and overlap (two-center) components. In that initial approach, it was assumed that each LMO, denoted as l, corresponded to a specific chemical bond A–B within a molecule. Based on this assumption, the overlap density at a spatial point $\vec{r}$ is computed from a single LMO, as outlined by the following expression:

$$\rho_{l,\mathrm{OP}}(\vec{r}) = \sum_{i\in A}^{m}\sum_{j\in B}^{m} c_{li}c_{lj}\phi_i(\vec{r})\phi_j(\vec{r}) \tag{1}$$

Here, ϕ_i represents the primitive or contracted functions, c_{li} are the LMO expansion coefficients, and m is the number of basis functions or atomic orbitals. This overlap component was then utilized to calculate various chemical bond descriptors, such as electron density, Coulomb repulsion, and polarizability. This was achieved by applying the appropriate operator to the overlap contribution, which was generated using a single LMO. Localization techniques, such as the well-known Pipek-Mezey localization [80], rely on atomic-charge based methods and may involve various types of charge partitions, including Mulliken, Bader, Becke, Löwdin, or Hirshfeld populations [81]. It is important to note that localization procedures can introduce bias into the overlap density when obtained for individual LMOs.

Therefore, in the present report, we demonstrate the direct acquisition of overlap density using MOs instead of LMOs.

To implement this approach, the single-particle density function can be calculated by evaluating the expectation value of the $\delta(\mathbf{r})$ operator [82], expressed as:

$$\rho(\mathbf{r}) = \int \psi(\mathbf{x}_1, \mathbf{x}_2, \ldots, \mathbf{x}_N)\delta(\mathbf{r})\psi^*(\mathbf{x}_1, \mathbf{x}_2, \ldots, \mathbf{x}_N)d\mathbf{x}_1 d\mathbf{x}_2 \ldots d\mathbf{x}_N \tag{2}$$

Here, $\psi(\mathbf{x}_1, \mathbf{x}_2, \ldots, \mathbf{x}_N)$ represents a normalized N-electron wavefunction, and $\delta(\mathbf{r})$ serves to probe the electrons at a specific point in space and can be expressed as the one-electron operator:

$$\delta(\mathbf{r}) = \sum_{i=1}^{N} \delta(\mathbf{r} - \mathbf{r}_i) \tag{3}$$

This operator sums over all electron arrangements $\mathbf{r}_i$ within the system, describing the electron density at each point $\mathbf{r}$ in space.

For a Hartree-Fock (HF) or DFT $|\varphi\rangle$ single determinant wavefunction, the total electron density at a point $\vec{r}$ in space is computed as follows:

$$\rho_{mol}(\vec{r}) = \sum_{l}^{M} n_l \sum_{i}^{m} \sum_{j}^{m} c_{li}c_{lj}\phi_i(\vec{r})\phi_j(\vec{r}) \tag{4}$$

l ranges in Equation (4) over all M MOs (spatial components of spin-orbitals), n_l represents the MO occupancy, m is the number of atomic orbitals (AOs), c_{li} denotes the AOs' expansion coefficients from the Linear Combination of Atomic Orbitals (LCAO), and ϕ_i corresponds to the primitive or contracted basis functions describing the AOs.

Without losing any information, the summations involving i and j in $\rho_{mol}(\vec{r})$ in Equation (4) can be decomposed into one-center and two-center contributions. This decomposition is applicable to a molecule with a structure element –R–A–B–R′–, where our primary interest lies in the chemical bond A–B, while R and R′ represent general molecular fragments. Considering $\rho^l_{MO_{ij}}(\vec{r}) = \sum_i^m \sum_j^m c_{li}c_{lj}\phi_i(\vec{r})\phi_j(\vec{r})$, the modified form of Equation (4) is expressed as follows:

$$\begin{aligned}\rho_{mol}(\vec{r}) \quad &= \sum_{l}^{M} n_l(\rho^l_{MO_{AA}}(\vec{r}) + 2\rho^l_{MO_{AB}}(\vec{r}) \\ &+ \quad \rho^l_{MO_{BB}}(\vec{r}) + \sum \rho^l_{MO_{others}})\end{aligned} \tag{5}$$

In Equation (5) $\rho^l_{MO_{AA}}(\vec{r})$ and $\rho^l_{MO_{BB}}(\vec{r})$ represent the one-center terms (with $i \in A$ and $j \in A$), and $\rho^l_{MO_{AB}}(\vec{r})$ is the two-center (overlap) term (with $i \in A$ and $j \in B$) of the l-th MO contribution to the total electron density. The terms $\rho^l_{MO_{others}}(\vec{r})$ represent the contributions of the remaining atoms in the molecule, which include other one-center and two-center terms, specifically: $\rho^l_{MO_{AR}}(\vec{r})$, $\rho^l_{MO_{AR'}}(\vec{r})$, $\rho^l_{MO_{BR}}(\vec{r})$, $\rho^l_{MO_{BR'}}(\vec{r})$, $\rho^l_{MO_{RR}}(\vec{r})$, and $\rho^l_{MO_{R'R'}}(\vec{r})$. Since we are specifically interested in the A–B bond, its overlap term is expressed for a single determinant as:

$$\rho_{AB}(\vec{r}) = 2\sum_{l}^{M} n_l \sum_{i\in A}^{m} \sum_{j\in B}^{m} c_{li}c_{lj}\phi_i(\vec{r})\phi_j(\vec{r}) \tag{6}$$

Equation (6) exclusively considers the two-center terms (when $i \in A$ and $j \in B$). $\rho_{mol}(\vec{r})$ in Equation (4) represents the one-particle density, typically determined by X-ray crystallographers [62], which solely involves terms of one electron (from the same spin-orbitals). $\rho_{AB}(\vec{r})$ in Equation (6) is a component resulting from a Mulliken-like decomposition of Equation (4) into atomic basis and does not encompass two-electron (electron pair) density terms [83].

2.2 | Overlap Density From MCSCF Wavefunctions

To obtain OP/TOP descriptors from an MCSCF wavefunction, the first step involves constructing what is referred to in the OP model as the overlap density, ρ_{OP}. To do this, we start from the configuration interaction (CI) expansion of the wavefunction:

$$|\psi\rangle = \sum_{\kappa} \mathbb{C}_\kappa \cdot |\varphi_\kappa\rangle \tag{7}$$

where $\mathbb{C}_\kappa$ are the CI expansion coefficients, and $|\varphi_\kappa\rangle$ represents different determinants. Taking $|\varphi_0\rangle$ as the HF-reference, the configuration interaction wavefunction $|\psi\rangle$ with singles and doubles excitations (CISD) can be expressed as:

$$|\psi\rangle = \mathbb{C}_0 \cdot |\varphi_0\rangle + \sum_{ra} \mathbb{C}^r_a \cdot |\varphi^r_a\rangle + \sum_{a<b, r<c} \mathbb{C}^{rs}_{ab} \cdot |\varphi^{rs}_{ab}\rangle \tag{8}$$

Here, $|\varphi^r_a\rangle$ is a single Slater determinant generated when spin-orbital a is replaced by spin-orbital r, and $|\varphi^{rs}_{ab}\rangle$ is the Slater determinant generated when spin-orbitals a and b are replaced by spin-orbitals r and s. The total electron density of the wavefunction expressed by Equation (8) is written as follows:

$$\begin{aligned}\rho(\mathbf{r}) \quad &= \langle\psi|\,\delta(\mathbf{r})\,|\psi\rangle \\ &= \sum_{\kappa\lambda} \mathbb{C}_\kappa \cdot \mathbb{C}_\lambda \cdot \langle\varphi_\kappa|\,\delta(\mathbf{r})\,|\varphi_\lambda\rangle\end{aligned} \tag{9}$$

where a significant number of Slater determinants must be considered. The matrix elements $\langle\varphi_\kappa|\,\delta(\mathbf{r})\,|\varphi_\lambda\rangle$ involve determinants that can be equal or may differ by one, two, or more spin-orbitals. Using the rules of Slater-Condon [84, 85] for matrix elements and considering the one-electron density operator, the evaluation of overlap between $\langle\varphi_\kappa|$ and $|\varphi_\lambda\rangle$ leads to the matrix elements $\langle\varphi_\kappa|\,\delta(\mathbf{r})\,|\varphi_\kappa\rangle$ and $\langle\varphi_\kappa|\,\delta(\mathbf{r})\,|\varphi_\lambda\rangle$. The latter is nonzero only when the interaction between determinants $\langle\varphi_\kappa|$ and $|\varphi_\lambda\rangle$ involves a difference of one spin-orbital [62], affecting the one-electron density.

The matrix elements $\langle\varphi_\kappa|\,\varphi_\kappa\rangle$ encompass all Slater determinants for the MCSCF wavefunction, as described in Equation (4), where $\mathbb{C}_k$ represents their expansion coefficients. It's important to note that Equation (9) simplifies to Equation (4) when considering only one determinant, with $\mathbb{C}_\kappa = 1.0$. Matrix elements $\langle\varphi_\kappa|\,\varphi_\lambda\rangle$ involve only the term with one different spin-orbital. By applying the same decomposition as in Equation (5) and utilizing Equation (6) for each matrix element, the overlap term (AB) takes the following form:

$$\rho_{\mathrm{AB}}(\vec{r}) = 2 \sum_{\kappa}^{\mathrm{SDs}} \mathbb{C}_{\kappa}^{2} \sum_{l}^{M_{\kappa}} n_l \sum_{i\in A}^{m} \sum_{j\in B}^{m} c_{li} c_{lj} \phi_i(\vec{r}) \phi_j(\vec{r}) + \sum_{\kappa\lambda}^{\mathrm{SDs}} \mathbb{C}_{\kappa} \mathbb{C}_{\lambda} \sum_{i\in A/B}^{m} \sum_{j\in B/A}^{m} c_{\kappa i} c_{\lambda j} \phi_i(\vec{r}) \phi_j(\vec{r}) \quad (10)$$

Here, $\mathbb{C}_k$ represents the CI expansion coefficients for the k-th Slater determinant (SD). The index l ranges over the M_k molecular orbitals (the spatial part of the spin-orbital) that constitute the k-th SD, with n_l denoting the occupancy of the l-th MO. $\phi_i(\vec{r})$ and $\phi_j(\vec{r})$ are atomic orbitals evaluated at position $\vec{r}$, while c_{li} and c_{lj} are their respective coefficients. The factor 2 on first term in right side of Equation (10) accounts for the possibilities of $(i \in A)(j \in B)$ and $(i \in B)(j \in A)$. Here, c_κ and c_λ denote the differing spin-orbitals within the pair of determinants $\langle\varphi_\kappa|$ and $|\varphi_\lambda\rangle$, respectively. It's notable that only spin-orbitals with the same spin contribute non-zero values in this context. In a CASSCF procedure, $\mathbb{C}$ and c coefficients are adjusted to obtain the total electronic wavefunction with the lowest possible energy. The expressions in Equations (9) and (10) strictly adhere to the approach adopted by many textbooks [62, 82] concerning the construction of the one-electron density matrix.

Also, NBOs can be employed to build the one-particle density matrix thus facilitating the extraction of the overlap density. This offers a more concise expression compared to the summations over determinants in Equation (10). In the ChemBOS package [35, 86], we have opted to retain the determinant form, mainly due to the inclusion of an OP/TOP descriptor not addressed in the context of the present work—the overlap polarizability [35, 37]. Calculating this descriptor involves a sum-of-states form, which can easily be implement into the current form of our ChemBOS software in the context of MCSCF and TDDFT when determinants are employed. It has to be emphasized that the numerical values of descriptors are not influenced by the chosen expansion.

It should be noted that, by definition, Equation (10) can be used for any CI expansion, including any multiconfigurational self-consistent field, multireference CI, or full-CI function. The only difference lies in the amount and quality of information that will be passed to our ChemBOS software (www.chembos.websitewww.chembos.website), which already has the functionality to use MCSCF wavefunctions. This functionality is available in a development version of ChemBOS that allows the reading of wavefunctions generated by program packages such as Gaussian [87] or Orca [88].

The overlap of atomic orbitals can lead to either constructive or destructive interference, affecting electron density across different regions of space. Nodes in molecular orbitals arise where destructive interference causes the contributions from overlapping atomic orbitals to cancel out, resulting in zero contribution to the total electron density from that molecular orbital at those nodes. The mutual orthogonality between molecular orbitals plays a crucial role in determining the presence and location of these nodes [89, 90], as it reflects the interference patterns formed during the combination of atomic orbitals. The presence of molecular orbitals with nodes, such as antibonding orbitals that exhibit nodes in the interatomic region, contributes to the overall electron density of the molecule. The presence or absence of these nodes influences electron concentration or depletion in the bonding region.

The spatial distribution of the overlap terms, as described by Equation (10), exhibits nodes and is characterized by positive and negative portions. These nodes, situated very close to the atomic positions, result in overlap density with regions of negative lobes, extending beyond the bonding region, and positive lobes, distributed within the bond region. Accordingly, $\rho_{OP}(\vec{r})$ is utilized in regions with positive values, while negative portions are considered as part of the atomic counterparts for the total electron density. This approach ensures the equality $\rho_{mol} = \rho_A + \rho_B + \rho_{\mathrm{OP}} + \rho_{\mathrm{rest}}$, where the last term refers to contributions from R and R' when considering an A–B bond in a system $R - \mathrm{A} - \mathrm{B} - R'$. To avoid the nodal and negative regions, the calculation of $\rho_{\mathrm{OP}}(\vec{r})$ involves numerically evaluating the expression given in Equation (10) at various grid points $\vec{r}$ in space. Only the positive (constructive combination) portion is considered, as explained in our recent reports [37, 45],

$$\rho_{\mathrm{OP}}(\vec{r}) = \rho_{\mathrm{AB}}(\vec{r}) \text{where} \vec{r} \in \{\vec{r} \,|\, \rho_{\mathrm{AB}}(\vec{r}) > 0\} \quad (11)$$

Furthermore, all numerical integrations are conducted with our Adaptive Subspace by Integral Importance (ASII) algorithm [86], which is an integral part of ChemBOS.

2.3 | Overlap Density Physical Meaning

The physical meaning of overlap can be interpreted as a manifestation of the interplay of the electronic effects contributing to the formation of a molecule. Levine and Head-Gordon [91], along with Martín and Francisco [92], provide an insightful discussion on the quantum mechanical origin of chemical bonds. The authors delve into the role of quantum mechanical interference and its connection to a reduction in kinetic energy when two approaching molecular fragments form a chemical bond. They use the overlap between the orbitals of each fragment as a common indicator of how the electron density responds to or influences various factors, such as kinetic energy reduction or increase, utilizing valence-core and core–core overlap to deduce kinetic energy reduction in bond formation for different systems. They further propose that the increase in kinetic energy can be attributed to the overlap of those orbitals which are principally involved in bonding with core orbitals.

Levine and Head-Gordon emphasize the importance of fragment interference and analyze the energetic contributions to bond formation. These authors establish a causal relationship in which the overlap of orbitals (considering MOs in their reported approach) defines the energetics of bond formation. Although the methodology proposed here does not provide any energy decomposition or aim to explain the interference phenomenon, it is noteworthy that the overlap of orbitals is frequently used to explain a variety of phenomena.

The overlap density (OP density in Equations 6, 10, or 11) presented in this work quantifies how all atomic orbitals overlap to form MOs, with the additional feature of decomposing the MOs densities into one-center and two-center contributions, with the OP density serving as the two-center portion in this decomposition.

2.4 | OP/TOP Descriptors

The central idea of the OP/TOP model is to use $\rho_{OP}(\vec{r})$ to access descriptors related to the chemical interaction between pairs of atoms. Here, we discuss four OP/TOP descriptors for the MCSCF wavefunction, namely: overlap density ρ_{OP}, intra-overlap Coulomb repulsion J_{OP}^{intra}, as well as the density ($\rho_{OCP}^{l}(\vec{r})$) and the Laplacian ($\nabla^2\rho_{OCP}^{l}(\vec{r})$) at the overlap critical point. These descriptors have been introduced previously [35, 37].

The **overlap density** ρ_{OP} is determined by integrating Equation (11) over the positive $\rho_{OP}(\vec{r})$ values. In our OP model, ρ_{OP} specifically represents the electron density shared between the atoms involved in a bond and is calculated as follows:

$$\rho_{OP} = \int_{-\infty}^{+\infty} \rho_{OP}(\vec{r})\, dv \approx \sum_{3Dgrid} \rho_{OP}(\vec{r})\Delta V \tag{12}$$

The integration is performed in real space, where dv and dV represent volume elements. To evaluate this integral, we employ an adaptive subspace scheme [86] for discretizing the 3D grid and conducting the integration, where ΔV represents the volume element of the corresponding numerical integration scheme.

The **intra-overlap Coulomb repulsion** J_{OP}^{intra}, within the context of the OP model, is defined as:

$$J_{OP}^{intra} = \int \rho_{OP}(\vec{r}_1) r_{12}^{-1} \rho_{OP}(\vec{r}_2) dr_1 dr_2 \tag{13}$$

r_{12} represents the distance between points r_1 and r_2 where the overlap densities $\rho_{OP}(\vec{r}_1)$ and $\rho_{OP}(\vec{r}_2)$ are examined. Typically, ρ_{OP} is higher for electron-rich chemical bonds. In the same vein, electron-rich chemical bonds that exhibit concentrated OP density in small regions tend to have higher J_{OP}^{intra} values.

Topological analysis of overlap density. Further insights into the shape of $\rho_{OP}(\vec{r})$ can be gained through a topological analysis of the OP density, similar to the QTAIM approach. This analysis aims to identify what are referred to as overlap critical points (OCP) [37]. In this context, two TOP descriptors have been recently introduced: the density at a chemical bond OCP, denoted as ρ_{OCP}, and its Laplacian, $\nabla^2\rho_{OCP}$. OCPs in chemical bonds exhibit all negative curvatures, which are calculated using the Hessian of the density at the OCP, represented as:

$$\mathbf{H}_{\rho_{OP}}^{OCP} = \begin{bmatrix} \frac{\partial^2\rho_{OCP}}{\partial x^2} & \frac{\partial^2\rho_{OCP}}{\partial x\partial y} & \frac{\partial^2\rho_{OCP}}{\partial x\partial z} \\ \frac{\partial^2\rho_{OCP}}{\partial y\partial x} & \frac{\partial^2\rho_{OCP}}{\partial y^2} & \frac{\partial^2\rho_{OCP}}{\partial y\partial z} \\ \frac{\partial^2\rho_{OCP}}{\partial z\partial x} & \frac{\partial^2\rho_{OCP}}{\partial z\partial y} & \frac{\partial^2\rho_{OCP}}{\partial z^2} \end{bmatrix} \tag{14}$$

Subsequently, $\mathbf{H}_{\rho_{OP}}^{OCP}$ is diagonalized to obtain the eigenvectors collected in Λ^{OCP} as follows:

$$\mathbf{H}_{\rho_{OP}}^{OCP} = \mathbf{P}\Lambda^{OCP}\mathbf{P}^{-1} \tag{15}$$

In this equation, $\mathbf{P}$ is a square 3×3 matrix, with its i-th column representing the eigenvector of $\mathbf{H}_{\rho_{OP}}^{OCP}$, and Λ^{OCP} is a diagonal matrix, with its diagonal elements as the corresponding eigenvalues, $\Lambda_{ii}^{OCP} = \lambda_i$. The Laplacian of the overlap density at the OCP is then defined as:

$$\nabla^2\rho_{OCP} = \lambda_1 + \lambda_2 + \lambda_3 \tag{16}$$

TOP descriptors provide insights into the shape of ρ_{OP}. Generally, a more localized overlap density ρ_{OP} leads to more negative $\nabla^2\rho_{OCP}(\vec{r})$ values and larger $\rho_{OCP}(\vec{r})$ [37].

2.5 | Quantum Theory of Atoms in Molecules

QTAIM bond critical point (BCP) descriptors [20–22] are employed here for comparison purposes. These descriptors include the total electronic density ($\rho_{r_{BCP}}$) and Laplacian ($\nabla^2\rho_{r_{BCP}}$) at a specific BCP, which provide insights into the charge concentration (higher $\rho_{r_{BCP}}$ values and $\nabla^2\rho_{r_{BCP}} < 0$) or depletion (lower $\rho_{r_{BCP}}$ values and $\nabla^2\rho_{r_{BCP}} > 0$) in the inter-atomic region [20].

In addition to these descriptors, the local energy density $H(r_{BCP})$ at a BCP, following the Cremer-Kraka criterion [93], is widely adopted as a measure of covalence. $H(r_{BCP})$ is defined as the sum of kinetic and potential energy density at the BCP: $H(r_{BCP}) = G(r_{BCP}) + V(r_{BCP})$. The potential energy contribution is stabilizing ($V(r_{BCP}) < 0$), while the kinetic energy is destabilizing ($G(r_{BCP}) > 0$). Therefore, BCPs with $H(r_{BCP}) < 0$ are expected to exhibit covalent character, whereas those with $H(r_{BCP}) > 0$ are indicative of ionic character or weak chemical interactions [93, 94]. It's important to note that although exceptions have been discovered regarding the characterization of ionicity and covalency based solely on the sign of $H(r_{BCP})$, these findings do not diminish the significance of assessing this bond descriptor [79, 95–98]. Analyzing the behavior of both $\nabla^2\rho_{r_{BCP}}$ and $H(r_{BCP})$ has proven to be a useful approach for describing the topology of chemical bonds within the framework of QTAIM [79].

2.6 | Local Vibrational Mode Theory

Normal vibrational modes within polyatomic systems are typically delocalized [99, 100]. This presents a significant challenge when one attempts to determine the intrinsic bond strength directly using normal mode frequencies and normal mode force constants. This is where LVM theory becomes invaluable. LVM, originally introduced by Konkoli and Cremer [101, 102] has transformed over the past decade into a powerful tool for the quantitative analysis of chemical bonds and/or weak chemical interactions for systems in the gas phase, solution and enzymes as well as for solid state systems. For a comprehensive review of LVM, including its theoretical foundation and wide-ranging applications in chemistry and beyond, readers are encouraged to explore two recent review articles and the references therein [28, 29].

The normal vibrational mode vector $\mathbf{d}_n$ expressed in internal coordinate q_n (where $n = 1, \cdots, N_{vib}$ and N_{vib} equals to $3N-6$ for a non-linear N-atomicsystem and $3N-5$ for linear N-atomic systems) and the diagonal normal mode force constant matrix $\mathbf{K}$

given in normal coordinates Q_n (both are found in the output of a standard normal mode analysis [103] is all what is needed to derive the corresponding local vibrational mode vector $\mathbf{a}_n$ that is associated with internal coordinates q_n through the following expression):

$$\mathbf{a}_n = \frac{\mathbf{K}^{-1}\mathbf{d}_n^{\dagger}}{\mathbf{d}_n\mathbf{K}^{-1}\mathbf{d}_n^{\dagger}}. \tag{17}$$

The calculation of the corresponding local mode force constant k_n^a can be performed using the following expression:

$$k_n^a = \mathbf{a}_n^{\dagger}\mathbf{K}\mathbf{a}_n. \tag{18}$$

Local mode force constants k^a have proven to be a reliable tool for quantifying the strength of a wide range of chemical bonds and/or weak chemical interactions [28, 29].

2.7 | Computational Procedure

All geometry optimization and frequency calculations were conducted using the Domain Based Local Pair Natural Orbital Coupled Cluster (DLPNO-CCSD(T)) method [104–106], utilizing the def2-QZVPPD basis set [107, 108] and the corresponding def2-QZVPPD/C auxiliary basis [109]. Numerical gradients were applied in all calculations.

The selection of the CAS active space was based on the Natural Orbital Occupation Numbers (NOON) [110] at the RI-MP2/SVP level of theory. NBOs with NOON values between 1.98 and 0.02 were adopted as active space. A wavefunction convergence test was performed for the H_2O molecule by increasing the active space from CAS(6,6) to CAS(6,30), using various basis sets including def2-TZVP, def2-TZVPPD, def2-QZVP, and def2-QZVPPD. DCD-CAS(6,6), DCD-CAS(6,8), and DCD-CAS(6,10) were also applied. These convergence tests were carried out based on the total dipole moment value and the overlap density descriptor. It should be noted that the geometry of the H_2O molecule optimized at the DLPNO-CCSD(T)/def2-QZVPPD level of theory was adopted for all CAS and DCD-CAS(2) convergence test calculations.

The X–O bond in X–OH or X–OF (where X = H, Li, Na, H_2B, H_3C, H_2N, HO, FO, F) and Li–X′ (where X = F, Cl, and Br) molecular test systems underwent analysis using CAS(10,16) (for H_2B–OH, H_3C–OH, H_2N–OH, HO–OH, and F–OH) and CAS(6,20) (for H–OH, Li–OH, Na–OH, Li–F, Li–Cl, and Li–Br). The dissociation profile of the Li–F bond was investigated using the CAS(2,6) method, along with its correction at the DCD-CAS(2) level of theory. The calculation of OP/TOP descriptors utilized CAS and DCD-CAS(2) (For Li–F) wavefunctions, whereas QTAIM counterparts were determined through CAS calculations for the molecules in equilibrion geometries. Since the equilibrium geometries of the test systems were determined using the DLPNO-CCSD(T)/def2-QZVPPD level of theory, the LVM analysis was also performed at the same level.

All geometry optimization, frequency calculations, CAS, and DCD-CAS(2) single-point calculations were conducted using Orca 5.0 [88]. OP/TOP descriptors were obtained using our ChemBOS software [35, 86],[1] while QTAIM descriptors were computed using Molden2aim [111] and MultiWFN [112] software. LVM analyses were performed using the LModeA package [113]. Details regarding Orca(*output*) → (*input*)ChemBOS conversion tools can be found in Figure S20 in Supporting Information.

3 | Results and Discussion

The OP/TOP descriptors were initially predicated from computed LMOs, where a single bond LMO was chosen as the exclusive molecular orbital (MO) for conducting the OP/TOP analysis. However, LMOs depend on atomic-charge based methods and may involve various charge partitions, which can influence each LMO and, consequently, the OP/TOP descriptors if these are obtained from individual LMOs. On the other hand, applying Equation (11) necessitates an MCSCF procedure in which both MO coefficients c_{li}, and determinant coefficients $\mathbb{C}_k$ are optimized. This implies the need to use canonical MOs instead of localized MOs due to the potential loss of the locality of LMOs after an MCSCF calculation. Therefore, demonstrating that the overlap density can be obtained from a canonical MO basis is crucial for extending OP/TOP descriptors from an MCSCF wavefunction. To address this, Figure 2 illustrates the equivalence between the overlap density derived from a single-determinant wavefunction (Equation 6) when utilizing a single localized MO (Figure 2a), spanning all LMOs (Figure 2b), and encompassing all canonical MOs (Figure 2c). The H_3C–OH bond was chosen, and the LMO associated with the pair of atoms C and O was specifically selected to construct the OP/TOP descriptors depicted in Figure 2a. Figure 2b,c, encompassing all LMOs or CMOs, respectively, were generated with a focus on the separation of overlap density between the selected atoms C and O.

When comparing OP/TOP descriptors using a single localized MO (Figure 2a) with those obtained spanning all LMOs (Figure 2b), it is evident that both ρ_{OP} and J_{OP}^{intra} are higher when employing a single localized MO. Additionally, ρ_{OCP} exhibits a similar behavior. Conversely, $\nabla^2\rho_{OCP}(\vec{r})$ assumes more negative values. This suggests a slightly higher charge concentration in the overlap density when a single localized MO is utilized, possibly due to the design of LMOs to maximize electron density locality. Furthermore, considering only one LMO to build the overlap density means that the nodal regions from other LMOs are not taken into account. These nodal regions contribute negatively to the total (and positively defined) electron density. Consequently, constructing the overlap density using only the bonding LMO may result in higher values of ρ_{OP}.

Figure 2b,c clearly demonstrate that the OP density remains invariant under general orbital unitary transformations. MO localization procedures, being unitary transformations, maintain the total electron density unchanged, and similarly, the OP density is found to be invariant to these transformations. In Figure 2d, the electron densities (total $\rho(\vec{r})$ and overlap $\rho_{OP}(\vec{r})$) profiles along the O–C bond axis are illustrated. It is evident that both the total electron density and the overlap portion are entirely equivalent when spanning all LMOs or CMOs, resulting in superimposed profiles along the O–C bond.

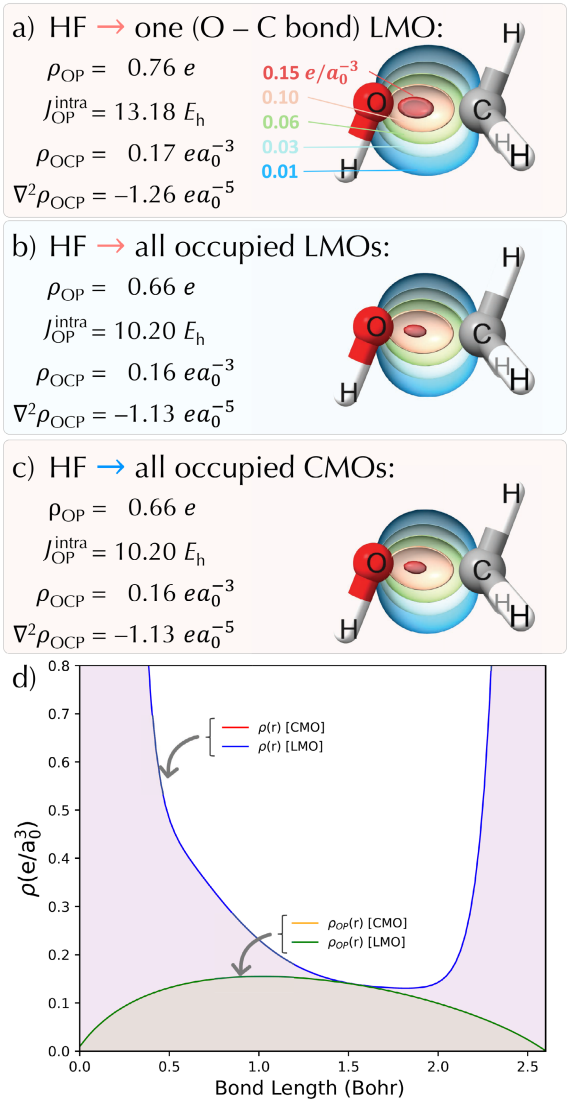

FIGURE 2 | OP/TOP descriptors for the O–C bond in H_3C–OH obtained using a single localized MOs (a), spanning all LMOs (b), and encompassing all canonical MOs (c). Panel (d) displays total ($\rho(\vec{r})$) and overlap ($\rho OP(\vec{r})$) electron densities (along O–C bond axis) spanning all LMOs/CMOs. $\rho_{OP}(\vec{r})$ maps in (a), (b), and (c) isosurfaces with contour values of 0.01, 0.03, 0.06, 0.10, and 0.15 e/a_0^3 were used in a red-green-blue color scheme, as indicated in (a). Calculations at the HF/def2-TZVP level of theory. The figures were generated utilizing the ChimeraX software [114–117], wherein a clipping plane was applied in the O–C bond planes.

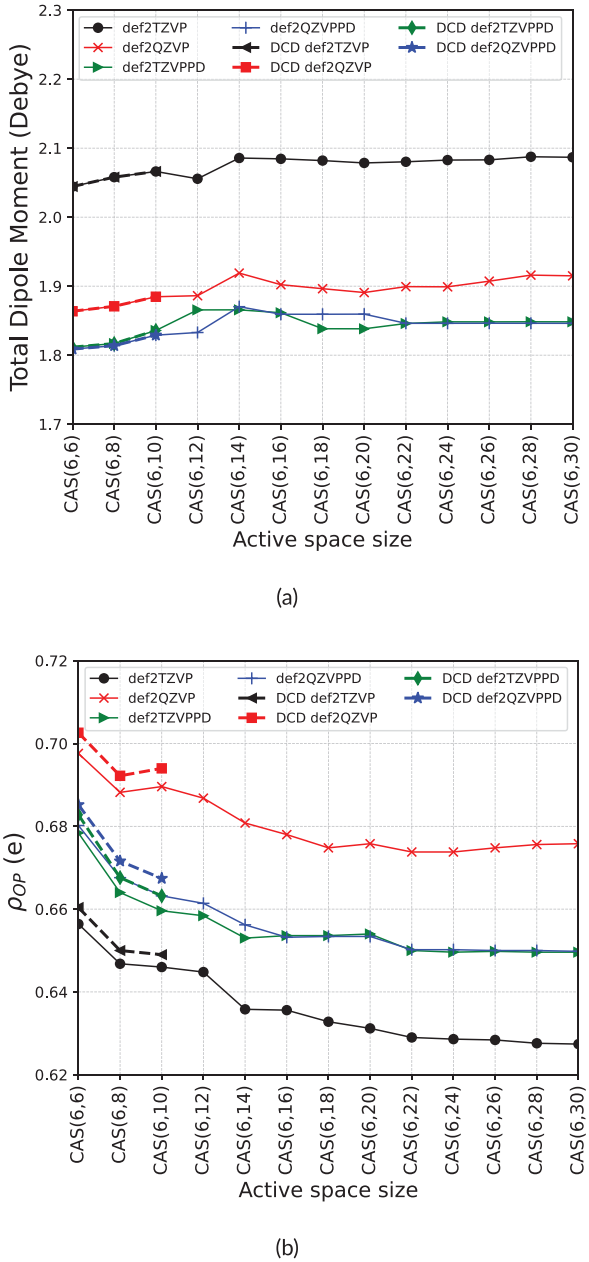

FIGURE 3 | Variations in molecular dipole moment (a) and O–H overlap density ρ_{OP} (b) with active space size in H_2O for different basis sets. The calculations were conducted using CASSCF active space sizes ranging from 6 to 30 and the DCD-CAS active space sizes from 6 to 10.

Interestingly, it is observed that the localized nature of the overlap density is maintained even when canonical MOs are utilized. This preservation of equivalence results in entirely similar OP/TOP descriptors, permitting the use of canonical MOs as a suitable basis for deriving the overlap density and its corresponding OP/TOP descriptors. While LMOs of any type could be employed for obtaining OP/TOP descriptors, CMOs are chosen here as the primary and straightforward option, widely adopted by various quantum chemistry packages. In the MCSCF procedure, the reference set of LMOs undergoes reoptimization, leading to a loss of their locality character. However, if the MOs resulting from the reoptimization of an initial set of LMOs maintain orthogonality, they can be utilized to construct the total electron density and obtain the OP density and its descriptors.

3.1 | Active Space Size Convergence

The convergence of CASSCF wavefunctions has been a subject of study for some time, and it's well-known that properties other than the energy converge with the active space size in a different manner than the energy [62]. Moreover, it has been established [118] that certain properties, such as the molecular dipole and polarizability, exhibit weak dependence on the size of the active space. It's important to note that even with a use of a large active space CASSCF may not recover a significant portion of dynamic

correlation. Even in cases where dynamic correlation is not dominant, it is crucial to test for each system under investigation CASSCF convergence with regard to increasing active space size and quality of basis set and their interplay. Figure 3 shows the molecular dipole moment (Figure 3a) and overlap density integral ρ_{OP} (Figure 3b) for different active spaces sizes and different basis sets.

It is observed that the inclusion of extra polarization and diffuse function at basis sets def2-TZVPPD and def2-QZVPPD leads to equivalent values of both dipole (CAS(6,22) and higher) and ρ_{OP} (CAS(6,16) and higher), with a value converging (1.846 Debye) to literature reference (1.864 Debye [119]). Interestingly, from CAS(6,16) to CAS(6,22), even with different molecular dipole moments, the overlap density integral for O–H bonds assume the same values for both def2-TZVPPD and def2-QZVPPD basis. The dynamic correlation corrected by the DCD-CAS method yields dipole moment values that are essentially the same as those obtained from the CASSCF counterparts up to CAS(6,10). A slight difference is observed in the ρ_{OP} values, but the trends remain similar. It is important to note that DCD-CAS was performed for an active space consisting of 6 electrons and up to 10 orbitals, due to the strong scalability of computational resource requirements with the number of determinants that DCD-CAS involves [78].

In addition to the observed convergence for the def2 basis set series, it is crucial to highlight some caveats. The achieved wavefunction convergence may not be replicated when utilizing other basis set families, such as Dunning's or Pople's basis sets. Figure 4 illustrates the electron density profiles (at CAS(6,30) level) along the O–C bond in H_3C–OH for Dunning's aug-cc-pVnZ (for n = D, T, Q), Pople's 6-311++G(2d*f*,2*p*), and def2QZVPPT basis sets. Additionally, the electron density difference maps among Dunning's basis sets are presented.

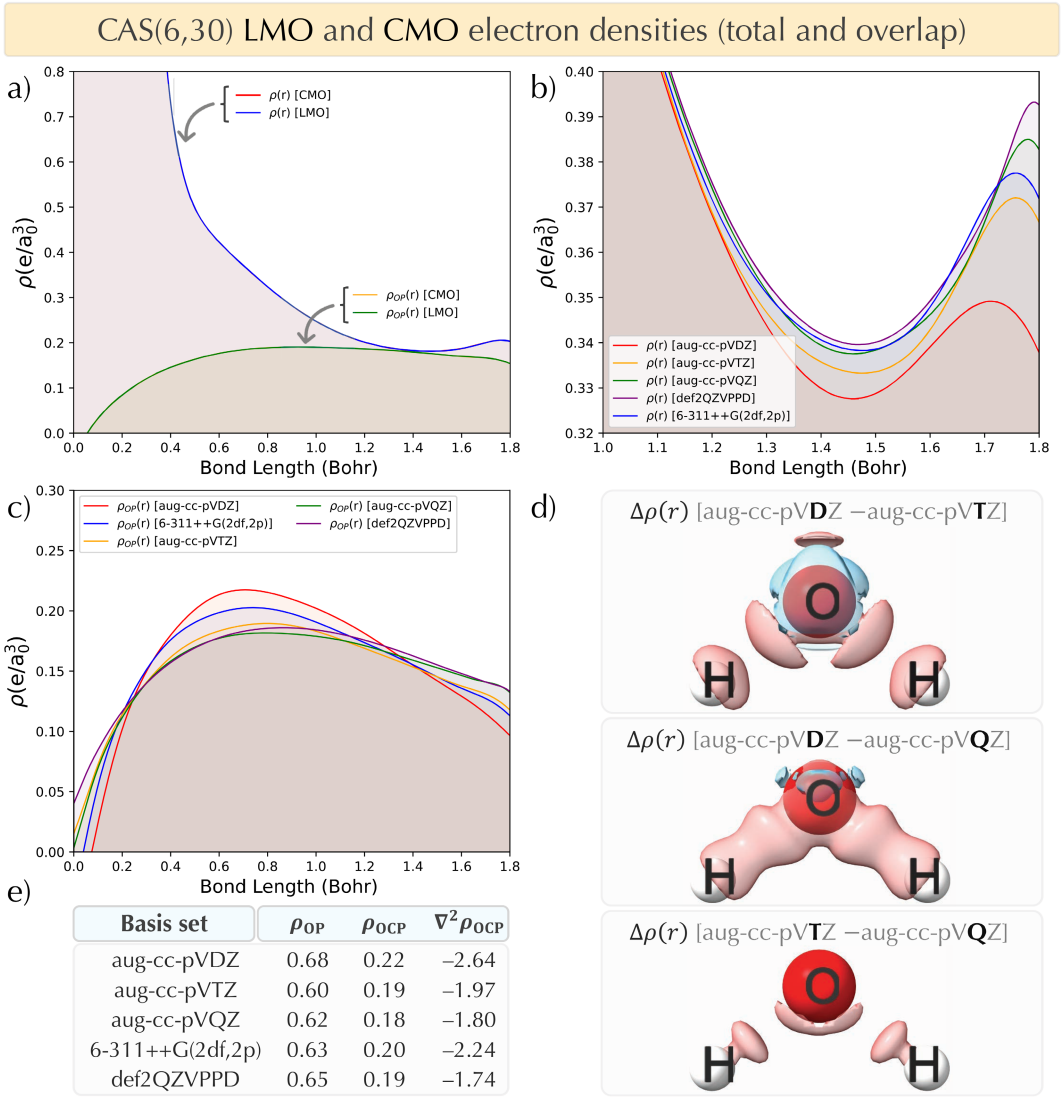

e)

Basis set	ρ_{OP}	ρ_{OCP}	$\nabla^2\rho_{OCP}$
aug-cc-pVDZ	0.68	0.22	–2.64
aug-cc-pVTZ	0.60	0.19	–1.97
aug-cc-pVQZ	0.62	0.18	–1.80
6-311++G(2df,2p)	0.63	0.20	–2.24
def2QZVPPD	0.65	0.19	–1.74

FIGURE 4 | (a) Profiles of total and overlap electron densities along the HO–H bond axis calculated at HF/def2QZVPPD, (b) and (c) respectively depict the total and overlap density profiles along the HO–H bond axis at CAS(6,30) level of theory using various basis sets. (d) Illustrates isosurfaces of the difference electron density ($\pm 0.006\, e\,/\,a_0^3$ in blue/red) obtained with different Dunning's basis sets within the CAS(6,30) framework. (e) Presents OP/TOP descriptors for various basis sets at the CAS(6,30) level. In (a), (b), and (c) profiles, the oxygen atom is on the left, and the hydrogen atom is on the right side.

First, in Figure 4a, the total and overlap electron densities constructed with canonical and localized MOs are shown, once again highlighting the invariance of OP density with MOs transformation. Additionally, in both Figures 2d and 4a, the elimination of contributions from one center to the total electron density can be observed. Naturally, heavier atoms exhibit increased atomic contributions. As it is not straightforward to perform CASSCF with LMOs as a starting point and maintain locality throughout the MCSCF procedure, Figure 4a was constructed for an HF wavefunction solely for the purpose of comparing the use of LMOs and CMOs in a system other than CH_3OH, specifically H_2O in this case.

Figure 4b illustrates profiles of the total electron density along the H–OH bond axis at the CAS(6,30) level of theory using various basis sets. It is evident that, with the progression from $n = $ D to Q in aug-cc-pVnZ basis sets, the total electron density undergoes significant changes in its distribution along the bond region, with a more pronounced impact close to the H atomic position. Additionally, in the bonding region, the basis sets aug-cc-pVQZ, 6-311++G(2*df*,2*p*), and def2QZVPPD lead to more similar density profiles. Figure 4d provides a 3D visualization of the density shifts corresponding to the changes in the basis set from $n = $ D to Q in aug-cc-pVnZ, highlighting a notable decrease in electron density in the bonding region characterized by the red isosurfaces ($-0.006e/a_0^3$).

Rappoport and Furche [107] emphasized that the adage "bigger is not necessarily better" holds true for diffuse basis set augmentation. These authors argued that finding the right balance between improved response properties and stability of the ground state can be difficult, particularly for smaller valence basis sets. Excessive diffuse augmentation may lead to issues such as spurious overpolarization, ill-conditioned overlap matrices, and a breakdown of integral prescreening and other low-order scaling methods. A fundamental tenet of def2 basis sets is the adoption of the smallest possible number of diffuse functions to mitigate these challenges.

Figure 4e provides a summary of OP/TOP descriptors for various basis sets at the CAS(6,30) level. Notably, OP/TOP descriptors sensitively reflect small variations in the electron density at the bond region, as measured by the OP density. It is emphasized that the OP density, being decomposed from atomic (one-center) contributions, is revealed to be more sensitive to changes in the basis set. It is important to highlight that the sensitivity lies not in the OP density being basis-set dependent but in its descriptors changing due to alterations in the total electron density caused by the change in the basis set.

The OP density is obtained by using orbitals expanded in atomic-centered bases and is partitioned in a Mulliken-like manner. Consequently, the intrinsic problems behind any Mulliken-like partition persist in our OP density. However, the main pitfall of a Mulliken-like partition is related to the excessive extension of diffuse functions when they are centered on one atom but reach a neighboring atom, artificially attributing electron density to the former atom. In the case of the OP density, we posit that adopting the overlap between atoms is mitigating this issue. This is primarily because we are not attributing any exponent that is centered on one atom (but pertains information from the neighbor atom) to that individual atom, but rather, we are considering exactly the shared contributions. This is evident as different basis sets, with a range of diffusion exponents, lead to similar OP density shapes.

An important aspect is that integrating Equation (10) yields the well-known Mulliken overlap population between atoms A and B. However, a significant distinction between Mulliken integrated overlap terms and the overlap model described here is that $\rho_{OP}(\vec{r})$ (as written in Equation 11) is utilized in regions with positive values, while negative portions are considered as part of the atomic counterparts for the total electron density. This approach ensures the equality $\rho_{mol} = \rho_A + \rho_B + \rho_{OP} + \rho_{rest}$, where the last term refers to contributions from R and R′ when considering an A–B bond in a system R–A–B–R′. Furthermore, it is worth noting that all descriptors offered by the OP model are not accessible through traditional Mulliken analysis, as demonstrated in recent literature employing the OP model [35, 37, 41, 45, 86, 120, 121]. Moreover, since the converged wavefunction is not influenced by any further basis set and/or active space extension, we can conclude that in this situation the overlap descriptor basis set and active space size dependencies are mitigated.

3.2 | QTAIM and LVM Trends in Test Systems

The chosen test systems represent various changes in the bonding situations arising from different chemical environments. Molecules numbered from **1** to **8** in Figure 1 encompass X–OH bonds with a diverse range of interaction classifications, encompassing polar covalent, charge-shift bonds, and ionic bond types (with increased multiconfigurational character calculated via the M-diagnostic—see Table S4). Fugel et al. [79] conducted a comprehensive analysis of these systems, primarily using DFT methodologies. Their bond analysis encompasses a wide range of bond descriptors, although it does not include OP/TOP and LVM descriptors. Additionally, it's worth noting that our test systems **1**, and **9**–**12** were not considered in Fugel's report.

Table 1 provides a comprehensive summary of the obtained results for each chemical bond descriptor across all test systems. Notably, all QTAIM results are consistent with those previously reported by Fugel et al. [79].

In general, for test systems **1**–**3**, it is observed that the H–O bond is the sole covalent bond, exhibiting both H_{BCP} and $\nabla^2\rho_{OCP}$ with negative values. These negative values indicate a shared interaction ($H_{BCP}<0$) and a bond charge concentration ($\nabla^2\rho_{OCP}<0$). In test systems **2** and **3**, the bond distance gradually increases, followed by a slight decrease in the already low values of $\rho_{r_{BCP}}$. From Li–OH to Na–OH bonds, there are low positive values for H_{BCP} and relatively high positive values for $\nabla^2\rho_{OCP}$, that decrease from Li to Na. This suggests that these bonds are primarily determined by electrostatic interactions and are characterized as ionic in nature. The local force constants of X–OH in test systems **1**–**3** qualitatively agree with bond distance, with k^a values decreasing as the bond distance increases, following the order $k^a(\text{H–OH}) > k^a(\text{Li–OH}) > k^a(\text{Na–OH})$.

TABLE 1 | Results for test examples **1–12** (see Figure 1): Bond distance r (in Å), overlap density ρ_{OP} (in e), intra-overlap repulsion J_{OP}^{intra} (in E_h), overlap critical point density ρ_{OCP} (in e/a_0^3), Laplacian of ρ_{OCP} at OCP $\nabla^2\rho_{OCP}$ (in e/a_0^5), electron density at BCP $\rho_{r_{BCP}}$ (in e/a_0^3), local energy density H_{BCP} (in E_h/a_0^3), Laplacian of $\rho_{r_{BCP}}$ (in e/a_0^5), and local bond stretching force constant k^a (in mDyn/Å). Calculations were performed at the CASSCF/def2-QZVPPD level of theory (details in Section 2.7).

No.	Bond	r	ρ_{OP}	J_{OP}^{intra}	ρ_{OCP}	$\nabla^2\rho_{OCP}$	$\rho_{r_{BCP}}$	H_{BCP}	$\nabla^2\rho_{r_{BCP}}$	k^a
1	H–OH	0.96	0.685	9.926	0.188	−1.796	0.370	−0.810	−2.860	8.400
2	Li–OH	1.59	0.905	11.526	0.108	−1.262	0.072	0.014	0.667	2.604
3	Na–OH	1.94	0.230	0.649	0.017	−0.174	0.051	0.011	0.430	1.877
4	H_2B–OH	1.35	0.749	12.000	0.165	−1.531	0.215	−0.195	1.029	6.479
5	H_3C–OH	1.42	0.577	7.749	0.137	−1.064	0.265	−0.426	−0.692	4.689
6	H_2N–OH	1.44	0.369	3.837	0.116	−0.865	0.294	−0.268	−0.372	4.294
7	HO–OH	1.45	0.280	2.369	0.101	−0.777	0.283	−0.204	0.020	5.595
8	F–OH	1.43	0.244	1.856	0.098	−0.899	0.280	−0.190	0.230	4.096
9	FO–OF	1.22	0.472	6.861	0.205	−1.929	0.557	−0.795	−1.048	4.320
10	Li–F	1.57	0.582	6.391	0.166	−3.440	0.077	0.014	0.718	3.891
11	Li–Cl	2.03	0.655	5.934	0.045	−0.216	0.044	0.005	0.276	1.401
12	Li–Br	2.18	0.665	5.641	0.033	−0.125	0.038	0.003	0.208	2.103

Test systems **4**–**8** demonstrate variations in the bond situations for X–OH with X ranging from B to F. The results are generally consistent with those reported by Fugel et al. [79], with some slight differences, likely attributable to the different computational methods (single- vs. multi-determinant) employed. As expected, B–O exhibits a positive $\nabla^2\rho_{BCP}$ and a negative H_{BCP}, characterizing it as a highly polarized covalent bond. In contrast, C–O and N–O are classified as polarized covalent bonds due to both $\nabla^2\rho_{BCP}$ and H_{BCP} being negative. The O–O bond shows a negative H_{BCP} and a positive, nearly zero $\nabla^2\rho_{BCP}$, which increases in the case of the F–O bond.

Test system **9** (FOOF) is known to exhibit multiconfigurational character (with a high M_{index} value, see Table S4 in the Supporting Information) and possesses unusual chemical properties. It has been reported [54] to have an atypical geometry with a very short O–O bond, approximately 1.22 Å, as a result of the anomeric effect, which delocalizes a π-type lone pair on oxygen into a low-lying σ^*(O–F) orbital. Consequently, the O–O bond in FOOF shows a high negative $\nabla^2\rho$BCP, indicating charge concentration in the bond region and a strong covalent character, with H_{BCP} being negative.

It's worth noting that both O–O (in HOOH) and F–O (in FOH) bonds are characterized as being stabilized by the resonance of ionic forms rather than the covalent sharing of electrons, known as charge-shift bonds (CSBs) [122]. A characteristic of CSBs is that the electron density between the bonded atoms is predicted to be low, which is not entirely reflected in the high values of $\rho_{r_{BCP}}$ for O–O and F–O bonds obtained from QTAIM. As CSB is inherently a multi-determinant concept, a deeper analysis of this behavior can be facilitated through a comparison of Hartree-Fock (single determinant) and CASSCF (including multi-determinants). Figure 5a,b provides OP/TOP descriptors for the O–O bond in HO–OH obtained using Hartree-Fock (Figure 5a) and CAS(10,16) (Figure 5b) wavefunctions, while Figure 5c depicts total ($\rho(\vec{r})$) and overlap ($\rho_{OP}(\vec{r})$) electron densities along the O–O bond axis. It is observed that the HF calculation, when compared with the CASSCF counterpart, results in an OP density that is more electron-rich (higher ρ_{OP}), with also higher J_{OP}^{intra}. The HF wavefunction also exhibits more negative $\nabla^2\rho_{OCP}$ and higher ρ_{OCP}.

Despite the prediction in CSBs that the electron density between bonded atoms is expected to be low, the CASSCF total electron density along the O–O bond axis is higher than the HF counterpart. This is probably a consequence of the ionic determinants taking place in the CASSCF procedure, which are not present in the HF calculation. Conversely, when considering the OP density, a decrease in ρ_{OP} when multi-determinantal effects take place is observed, aligning with the resonance of ionic forms rather than the covalent sharing of electrons idea of CSBs. A more detailed analysis of the relationship between OP descriptors and CSBs can be found in the literature [35]. Essentially, using DFT-based OP densities, it was found that larger CSBs resonance energies were associated with more compact overlap densities. A further analysis on this subject using MCSCF, despite being relevant, is outside the scope of the present report.

The comparison presented in Figure 5 also serves as a compelling example highlighting the motivation for the effort involved in transitioning from monodeterminantal to multi-determinantal wavefunctions when studying chemical bonds, even for small systems.

From the perspective of LVM theory, the local force constants decrease in the series from B to F, with the exception of the HO–OH case, which exhibits an increased k^a value. In this sense, the O–O bond is stronger than the C–O and N–O bonds in test systems **5** and **6**, and the O–O bond in test systems **9**.

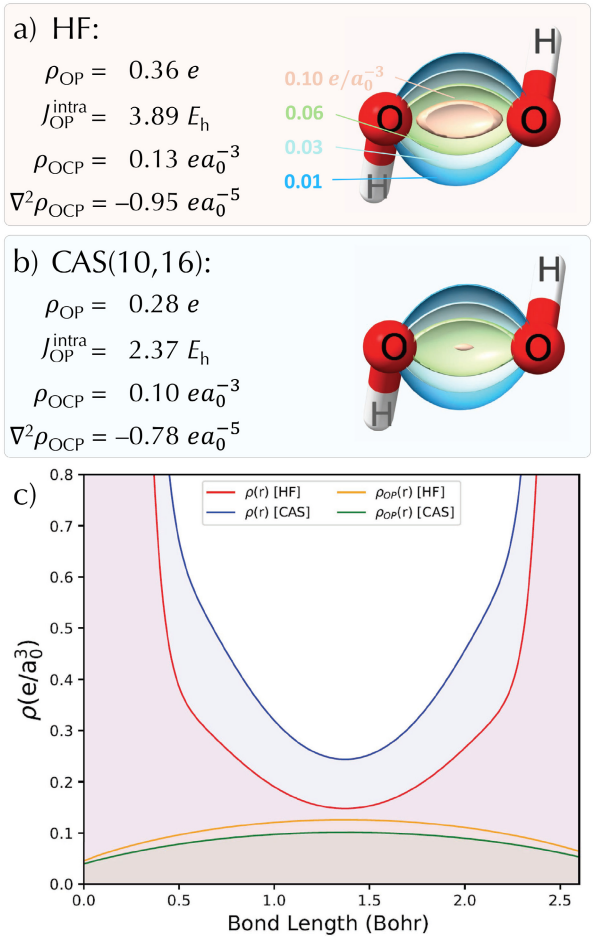

FIGURE 5 | OP/TOP descriptors for the O–O bond in HO–OH obtained using Hartree-Fock (a) and CAS(10,16) (b) wavefunctions. Panel (c) displays total ($\rho(\vec{r})$) and overlap ($\rho_{OP}(\vec{r})$) electron densities along O–O bond axis. $\rho_{OP}(\vec{r})$ maps in (a) and (b) ranging from 0 to 0.16 e/a_0^3 in a red-green-blue color scheme. Calculations using def2QZVPPD basis set. The figures were generated utilizing the ChimeraX software [114–117], wherein a clipping plane was applied in the O–O bond planes.

Test systems **10**–**12** (Li–F, Li–Cl, and Li–Br) exhibit small and positive ρ_{BCP} and H_{BCP}, both decreasing along the series. Additionally, the high and positive $\nabla^2\rho r_{BCP}$ value also decreases along this series. These values indicate charge depletion in these bonds ($\nabla^2\rho_{r_{BCP}}>0$) and major electrostatic interactions ($H_{BCP}>0$). The local force constants for test systems **10**–**12** agree with the normal mode force constants, but their behavior does not follow either the bond distances or the QTAIM descriptors.

3.3 | OP/TOP Descriptors for the Studied Molecules

Considering the performance and computational demands of CASSCF calculations for OP/TOP descriptors is crucial. These calculations are notorious for their time-consuming nature, with computational resources scaling notably with basis set size and active space [123]. For instance, a CAS(6,6) calculation generates 141 Slater determinants, while a CAS(6,30) calculation produces around 1.4×10^6 Slater determinants, illustrating the challenge of larger active spaces (see Figure S1 in Supporting Information). Despite this, once converged, the number of Slater determinants required for accurate wavefunction description varies by system. Our implementation in ChemBOS efficiently handles Slater determinants with strong parallel performance. For instance, in a CASSCF(6,6)/def2-QZVPPD calculation for H_2O, ChemBOS achieves a remarkable speedup of approximately 105 when run with 128 threads on an AMD EPYC 7763 with 512 GB of RAM (details in Figure S16 in Supporting Information).

The increase in bond polarization, as captured by QTAIM through $\nabla^2\rho_{r_{BCP}}$ and H_{BCP} descriptors, is interpreted as a decrease in covalent character. This aligns with the well-established Bent's rule [124], which posits that bonds between elements of varying electronegativities tend to be polar, causing the electron density in such bonds to shift towards the more electronegative element. Recently, Alabugin, Bresch, and Manoharan [125] used a polarization percentage (Pol%) calculated as the square of natural hybrid orbital (NHO) coefficients in the bonding NBOs from MP2/6-311++G(*d*,*p*) level of theory and reported results consistent with Bent's rule, showing that polarization towards X (in H_nX–OH) bonds increases from B–O to F–O.

In a similar vein, other chemical bond descriptors are anticipated to yield chemically meaningful values that align with these trends. According to the OP model, chemical bonds formed between atoms with different electronegativities are likely to exhibit overlap density ($\rho_{OP}(\vec{r})$) shifted towards the more electronegative atom. Profiles of $\rho_{OP}(\vec{r})$ along the bond axis for test systems **1**–**12** are presented in Figure 6.

It is evident that $\rho_{OP}(\vec{r})$ tends to be more concentrated around the most electronegative atom and less dispersed in the bonding region, consistent with the expected behavior. ρ_{OP} represents the two-center contribution of a specific bond to the total one-electron density and generally has higher values for electron-rich chemical bonds. This trend is also evident in Table 1 and Figure 6. Across all subgroups (test systems **1**–**3**, **4**–**8**, and **10**–**12**), the overlap critical point density (ρ_{OCP}) decreases as one transitions from H to Na in O–X bonds for test systems **1**–**3**, from B to F in test systems **4**–**8**, and from F to Br in Li–X bonds for test systems **10**–**12**.

In the series of alkali (and hydrogen) hydroxides (test systems **1**–**3**), the H–O bond stands out with the highest ρ_{OCP} and $\nabla^2\rho_{OCP}$ values, even though it doesn't have the highest ρ_{OP} and J_{OP}^{intra} values when compared to the Li–OH bond. This distinction arises from the inherently polar covalent nature of the H–O bond, as revealed by the QTAIM analysis. Additionally, hydrogen (H) lacks core electron shells, which further contributes to these differences. Consequently, the overlap density in H–O bond is distributed throughout the entire bond region but predominantly concentrates along the bond axis (as depicted in the gray plot in Figure 6a). As we progress down the Periodic Table, moving from Li to Na, a significant decrease in overlap density becomes evident, primarily due to the heightened ionic character of these bonds. 2D color maps of the overlap density for test systems **1**–**3** are available in the Supporting Information.

In test systems **4**–**8**, the B–O bond, which has the highest ρ_{OCP} in the series and is less spread (exhibiting the most negative

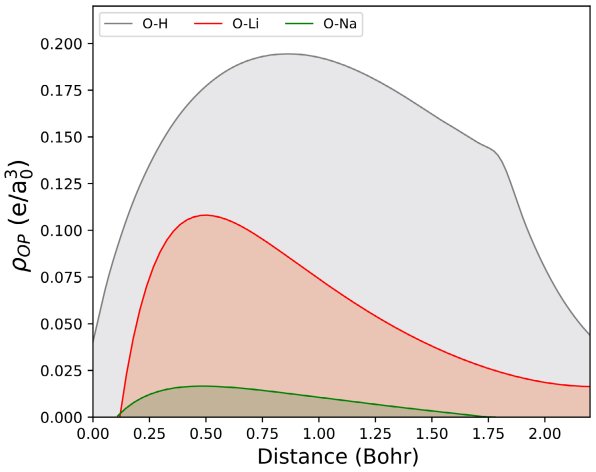

(a)

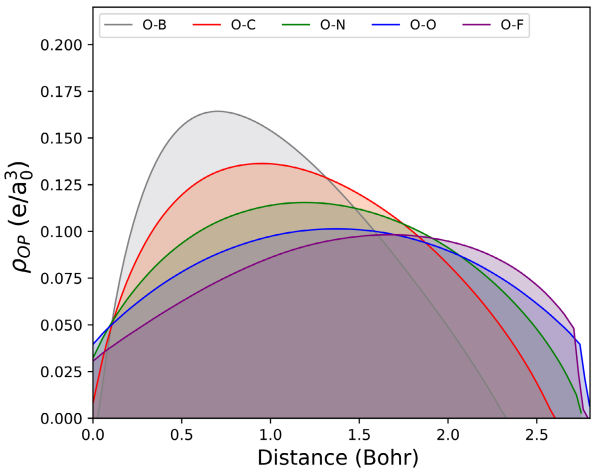

(b)

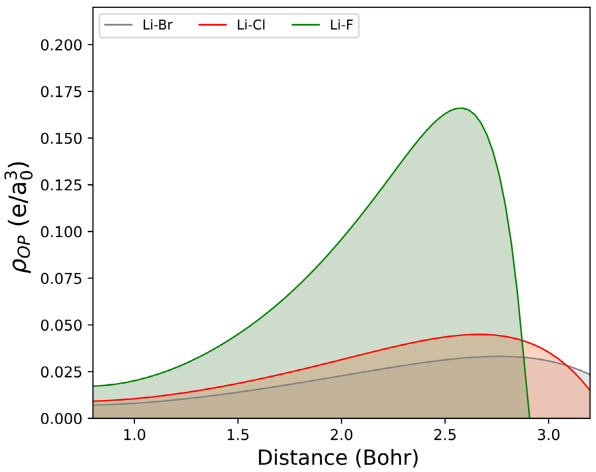

(c)

FIGURE 6 | Profiles of $\rho_{OP}(\vec{r})$ along the bond axis for test systems **1**–**11**. In plots (a) and (b), the oxygen atoms are depicted on the left side, while in plot (c), it is the lithium atom. Calculations were performed at the CASSCF/def2-QZVPPD level of theory (details in Section 2.7).

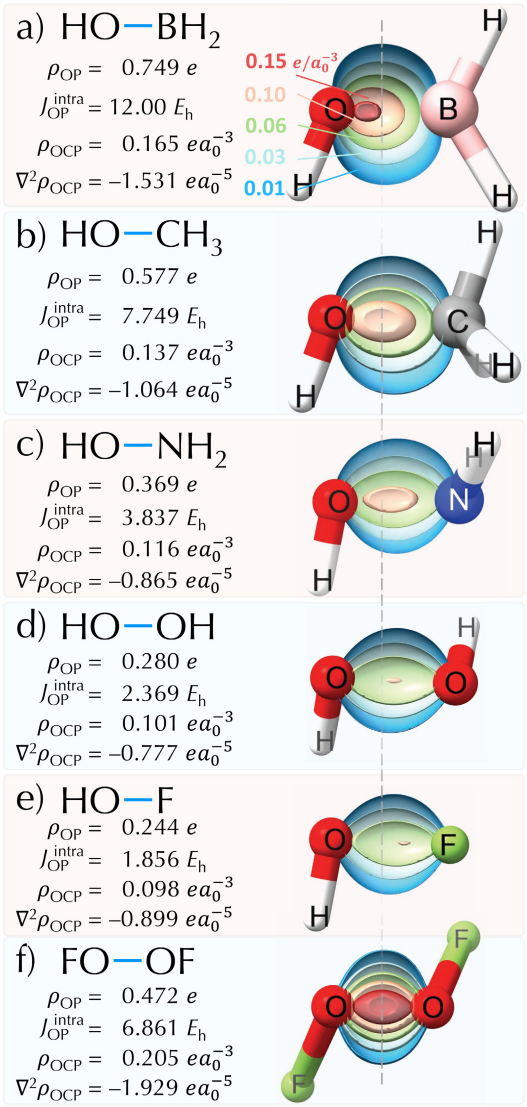

FIGURE 7 | OP/TOP descriptors and $\rho_{OP}(\vec{r})$ maps for O–X bonds, where X = BH_2, CH_3, NH_2, OH, and F. Isosurfaces with contour values of 0.01, 0.03, 0.06, 0.10, and 0.15 e/a_0^3 were used in a red-green-blue color scheme, as indicated in (a). Calculations were performed at the CASSCF/def2-QZVPPD level of theory. The figures were generated utilizing the ChimeraX software [114–117], wherein a clipping plane was applied in the C–X bond planes.

$\nabla^2\rho_{OCP}$), also exhibits the largest J_{OP}^{intra}. The qualitative scenario of overlap charge spreading across the chemical bond is quantified by the ρ_{OCP} and $\nabla^2\rho_{OCP}$ descriptors, indicating less spread (i.e., less negative $\nabla^2\rho_{OCP}$) bonds from C–O to F–O, as illustrated in Figures 6b and 7.

Figure 7 is equipped with lines that pass through the middle of the bonds, aiding the visualization of bond overlap density polarization towards the more electronegative atom. An observable trend is the gradual decrease in the values of ρ_{OP}, ρ_{OCP}, and J_{OP}^{intra} as we progress from B–O to F–O. Notably, $\nabla^2\rho_{OCP}$ becomes less negative up to O–O, but then increases for the F–O bond. Local bond stretching (k^a) inversely follows the trend of $\nabla^2\rho_{OCP}$, decreasing along the series but inverting the behavior

for HO–OH. It's interesting to note that QTAIM does not align with the trends observed in both OP/TOP and LVM analyses.

It's interesting to note that QTAIM indicates that the B–O bond is associated with a relatively high negative value of H_{BCP}, which Fugel et al. [79] attributed to the additional orbital overlap arising from the B–O π bond. The ρ_{OP} values in Table 1 take into account the overlaps between all MOs of different shapes in a multiconfigurational fashion, and indeed, the B–O bond exhibits a high ρ_{OP} value, which can be attributed to the extra stabilization of this bond. This extra stabilization is also supported by LVM analysis, which identifies the B–O bond as the strongest in the series of test systems from B–O to F–O.

Test system **9** exhibits a dihedral angle of 88.2°, which is close to 90°. Kraka and collaborators [54] reported that this conformation reduces lone pair-lone pair repulsion in the FOOF molecule. This dihedral arrangement facilitates the delocalization of the π-type lone pairs on oxygen into a low-lying σ^*(OF) orbital via the anomeric effect. Bridgeman and Rothery [126] also noted that the balance between F–O orbital repulsion and the O–O bond explains the anomalously long F–O and short O–O bond distances. In general, F–O single bonds are destabilized and lengthened due to repulsion between the lone pairs on fluorine atoms and the π orbitals of the O–O bond, a phenomenon not observed in HOOH. From the perspective of the OP/TOP model, the balance between different repulsive interactions, lone-pair delocalization, and lone-pair interaction with other orbitals increases the O–O overlap density (see Figure 7f), which is clearly reflected in the overlap descriptors.

In test systems **10**–**12**, which include Li–F, Li–Cl, and Li–Br bonds, the same trend as in the other test system groups is observed, where ρ_{OP} increases with increasing covalency or decreasing ionicity. However, there is an interesting difference between these two groups of systems. In test systems **1**–**8**, higher values of ρ_{OP} are generally followed by high values of J_{OP}^{intra}. In test systems **10**–**12**, on the other hand, we notice that as ρ_{OP} increases, J_{OP}^{intra} decreases.

A more detailed analysis of TOP descriptors reveals that in the Li–X series, where X ranges from F to Br, the variation in $\nabla^2\rho_{OCP}$ is much more pronounced. For example, it is $-3.440\ e/a_0^5$ for Li–F and $-0.125\ e/a_0^5$ for Li–Br. Essentially, as we move from Li–F to Li–Br, the overlap density becomes significantly more spread along the bond region, as measured by $\nabla^2\rho_{OCP}$ (as seen in Figure 6c). This leads to a drop in J_{OP}^{intra} even though there is an increase in the overlap density integral.

3.4 | OP/TOP Descriptors Li–F Bond Dissociation

We have chosen the dissociation pattern of the Li–F bond to highlight the differences in OP/TOP descriptors when utilizing CASSCF and a second-order corrected wavefunction, specifically the Orca implementation DCD-CAS(2). The primary aim is to demonstrate that even a partial correction addressing dynamic correlation in the wavefunction leads to differences in the OP density and its descriptors. Notably, in this Li–F example, a proper treatment of dynamic coupling is known to be mandatory, especially as one approaches the dissociation point in Li–F.

We utilized a state-averaged CAS(2,6) wavefunction, giving equal weights to the ground and first excited states. This active space includes the molecular orbital mainly composed of a p_z orbital located on the F atom, with small contributions from Li s-type atomic orbitals (illustrated in Figure 8a and referred to as MO-A), and a σ-type orbital primarily composed of Li s-type orbitals with small contributions from F*s*- and p_z-type atomic orbitals (depicted in Figure 8b and referred to as MO-B), among others.

At the equilibrium geometry, which is close to 1.5 Å, the ground state is primarily characterized by the Slater determinant involving MO-A, with a doubly occupied status. The Slater determinant composed of MO-B at a Li–F distance of 1.5 Å has negligible weight. However, as the dissociation of the Li–F

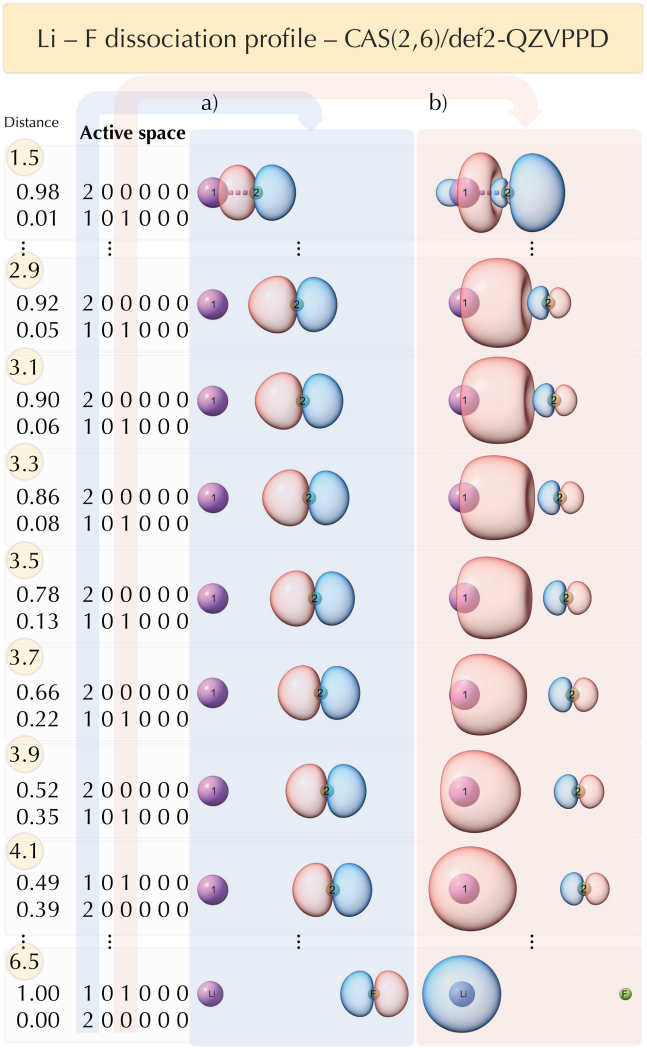

FIGURE 8 | Visualization of the two primary molecular orbitals (MOs) constituting the CAS(2,6) wavefunction during the Li–F dissociation process. Label 1 refers to Li and 2 to F atom. MO (a) is predominantly composed of F p_z-type atomic orbitals, while MO (b) is mainly derived from Li s-type atomic orbitals. Each box corresponds to a specific distance along the Li–F dissociation, displaying CASSCF coefficients and information about the compositions of Slater determinants. The numbers within each Slater determinant denote the occupation of the respective MO, with blue representing (a) and red representing (b). MOs are depicted with isosurfaces set at $0.05\ e/a_0^3$.

molecule proceeds, both the weights (CASSCF coefficients) and MO shapes undergo significant changes. MO-A gradually loses its Li s-type character, while the weight of the Slater determinant involving both MO-A and MO-B as single occupied orbitals increases. As depicted in Figure 8, at approximately 4.1 Å, an inversion in weights occurs, with the Slater determinant where both MO-A and MO-B are singly occupied having the larger coefficient. At greater distances (6.5 Å in Figure 8), MO-A is characterized by a pure $2p_z$ orbital at the F atom, while MO-B exhibits a pure 2s orbital at the Li atom. At this point, it can be considered that two neutral species are formed, with each MO having one electron.

It's important to mention that CASSCF calculations usually predict an avoided crossing point (between ground and excited states energies) at a distance of approximately 4.1 Å, as reported in previous studies [78, 127]. In contrast, a Full CI reference indicates an avoided crossing occurring at roughly 6.6 Å [128], and DCD-CAS(2) calculations with a CAS(2,2) active space result in a crossing point at 5.65 Å [78].

While the CASSCF (or other more accurate) wavefunction coefficients provide valuable insights into the ionic/ neutral nature of the chemical species, it is equally important to evaluate how chemical bond descriptors capture the changes in the wavefunction as a bond is broken. In this context, Figure 9 presents OP/TOP descriptors along the dissociation profile of the Li–F ground state using the CAS(2,6) wavefunction, as well as its correction at the DCD-CAS(2) level of theory. These curves focus on the range of 3.0 to 6.5 Å, covering the crossing points for both CASSCF and DCD-CAS(2) wavefunctions. Generally, for a given distance, the DCD-CAS(2) wavefunction yields higher values of ρ_{OP}, ρ_{OCP}, and J_{OP}^{intra} compared to the CASSCF counterpart. Additionally, $\nabla^2\rho_{OCP}$ is more negative with the DCD-CAS(2) wavefunction.

It is worth noting that OP/TOP descriptors sensitively reflect the ionic/neutral inversion in each type of wavefunction along the Li–F dissociation profile. Figure 9c shows that ρ_{OCP} drops to nearly zero precisely at the Li–F distance of 4.1 Å, the point at which the inversion occurs. J_{OP}^{intra} and $\nabla^2\rho_{OCP}$ approach zero for

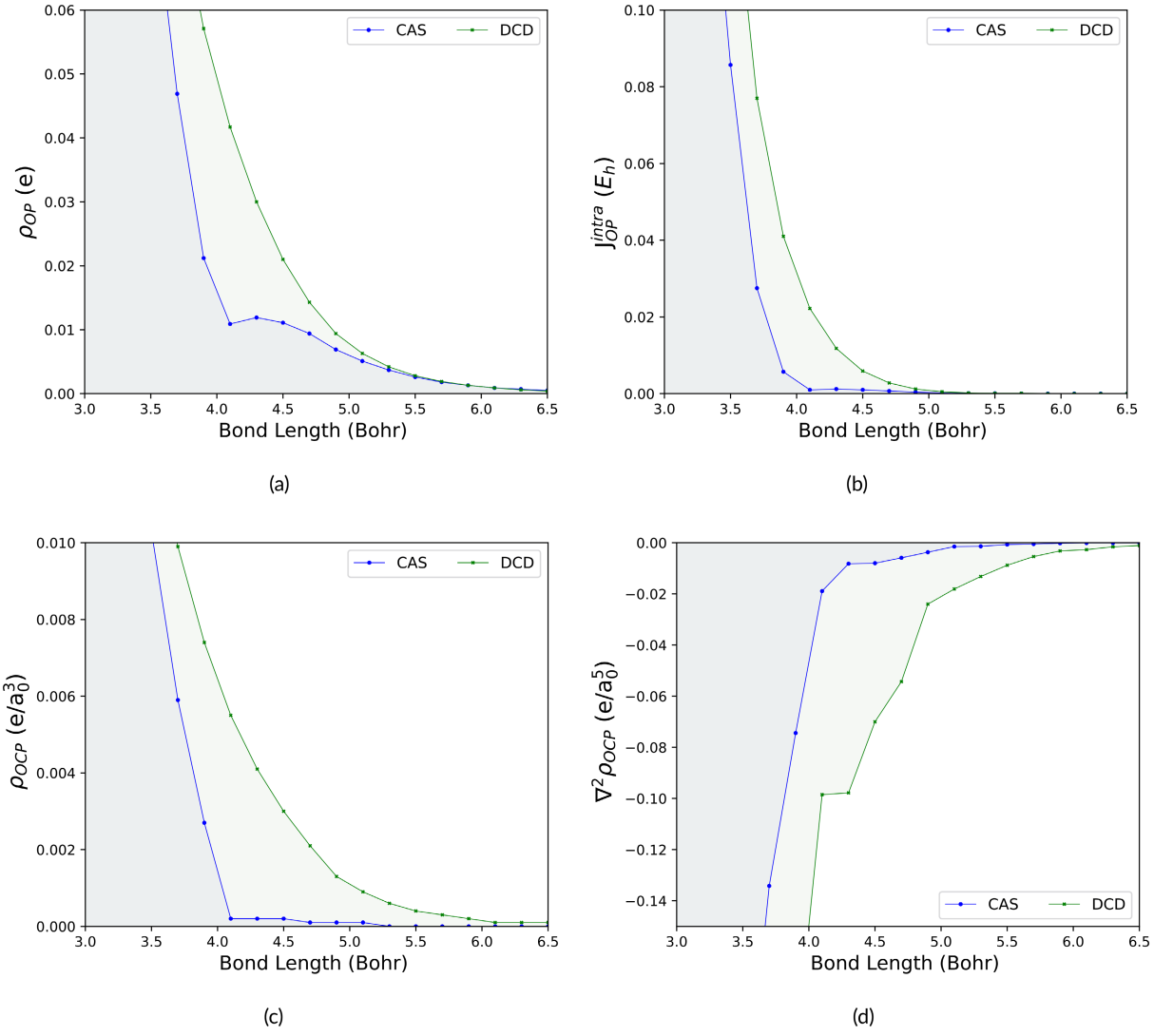

FIGURE 9 | OP/TOP descriptors: (a) ρ_{OP}, (b) J_{OP}^{intra}, (c) ρ_{OCP}, and (d) $\nabla^2\rho_{OCP}$ for Li–F bond dissociation profile using CASSCF(2,6) and DCD-CASSCF(2,6) wavefunctions.

distances above 4.1 Å. The overlap density integral exhibits an interesting behavior. It experiences a significant decrease near 4.1 Å, but then ρ_{OP} gradually decreases, becoming similar to the DCD-CAS(2) counterpart at a Li–F distance of 5.5 Å. This indicates that even when the neutral determinant dominates (with neutral Li having one electron in the 2s orbital and neutral F with a hole in the 2pz orbital), there is still some orbital overlapping occurring.

Both CASSCF and DCD-CAS(2) yield ρ_{OP} values that approach zero at approximately 6.5 Å. Specifically, for the CAS(2,6) wavefunction, ρ_{OP} vanishes close to 4.1 Å, whereas for the DCD-CAS(2) counterpart, this occurs near 6.1 Å. The disparity in the zero points of ρ_{OP} and ρ_{OCP} suggests a widely distributed overlap density, with its maximum critical point close to zero but still maintaining integrated overlap density. These insightful details about the MCSCF wavefunction, as provided by OP/TOP, can pave the way for novel applications in understanding chemical bond dynamics across various multiconfigurational and multireference classes of wavefunctions. Certainly, methodologies such as FullCI, MRCI, or other more robust approaches that account for dynamic coupling would result in a more accurate wavefunction and, consequently, more precise OP descriptors. It's crucial to recognize that with OP density descriptors, the accuracy is inherently tied to the quality of the wavefunction. While the ChemBOS implementation readily accommodates these methodologies, it's important to note that they are beyond the scope of the present report.

4 | Conclusions

In conclusion, this study delved into the realm of chemical bond descriptors, focusing on the extension of OP/TOP descriptors based on MCSCF wavefunctions. Through a comparative analysis of CASSCF wavefunctions for various molecular systems, including the X–O and Li–X′ test systems, we gained valuable insights into the behavior of these descriptors. The OP density invariance under general orbital unitary transformations offers a practical approach to compute overlap densities and OP/TOP descriptors accurately. Furthermore, the results highlighted the importance of converged wavefunctions in achieving precise property calculations.

Our investigation encompassed a broad spectrum of molecular systems, including X–O bonds in X–OH and Li–X′ interactions, each subjected to CAS(10,16) and CAS(6,20) calculations. These analyses challenged the MCSCF-based OP/TOP bond descriptors, offering valuable insights and allowing for comparisons with QTAIM and LVM descriptors. OP/TOP descriptors, guided by the OP model, demonstrated that chemical bonds formed between atoms with differing electronegativities tend to exhibit overlap density shifted towards the more electronegative atom. This effect was quantified using ρ_{OCP} and $\nabla^2\rho_{OCP}$ descriptors, which indicated reduced spreading (i.e., less negative $\nabla^2\rho_{OCP}$) in bonds with increasing electronegativity differences.

Additionally, our analysis of the Li–F dissociation profile revealed that OP/TOP descriptors sensitively reflected the ionic/neutral inversion along the Li–F dissociation pathway. The overlap density integral exhibited a distinctive behavior, experiencing a significant decrease near 4.1 Å, followed by a gradual decrease in ρ_{OP}, aligning with the DCD-CAS(2) counterpart at a Li–F distance of 5.5 Å. The analysis of ρ_{OCP} and $\nabla^2\rho_{OCP}$ along the dissociation pathway suggests a widely distributed overlap density near the ionic/neutral inversion. This intriguing observation suggests that even when the neutral determinant dominates, with neutral Li possessing one electron in the 2s orbital and neutral F exhibiting a hole in the 2pz orbital, some degree of orbital overlap persists.

Notably, OP/TOP descriptors provided unique perspectives on chemical bond dynamics, particularly in the context of multiconfigurational and multireference wavefunctions. The sensitivity of OP/TOP descriptors to ionic/neutral inversion during Li–F dissociation showcases their potential to elucidate different bonding phenomena. Our findings open the door to novel applications targeting a deeper understanding of chemical bond dynamics across diverse wavefunction classes and further advancing our comprehension of molecular properties and chemical interactions.

Acknowledgments

The authors are grateful for the financial support from CNPq and CAPES agencies. The authors thank the SMU O'Donnell Data Science and Research Computing Institute for generously providing computational resources. This work was funded by the Brazilian National Council for Scientific and Technological Development—CNPq, Grant numbers 406483/2023-0, and 310988/2023-3; Public Call n. 03 Produtividade em Pesquisa PROPESQ/ PRPG/UFPB project number PVN13305-2020 and CAPES Demanda Social 88887.659768/2021-00 and the National Science Foundation NSF, Grant CHE 2102461.

Conflicts of Interest

The authors declare no conflicts of interest.

Data Availability Statement

The data that support the findings of this study are available from the corresponding author upon reasonable request.

Endnotes

[1] Available at www.chembos.website.

References

1. G. N. Lewis, "The Atom and the Molecule," *Journal of the American Chemical Society* 38, no. 4 (1916): 762–785.

2. R. P. Feynman, "Forces in Molecules," *Physics Review* 56 (1939): 340–343.

3. C. A. Coulson, "The Contributions of Wave Mechanics to Chemistry," *Journal of the Chemical Society* (1955): 2069–2084.

4. L. Pauling, "The Nature of the Chemical Bond—1992," *Journal of Chemical Education* 69, no. 7 (1992): 519.

5. T. H. Dunning, M. S. Gordon, and S. S. Xantheas, "The Nature of the Chemical Bond," *Journal of Chemical Physics* 158 (2023): 130401.

6. L. Zhao, S. Pan, N. Holzmann, P. Schwerdtfeger, and G. Frenking, "Chemical Bonding and Bonding Models of Main-Group Compounds," *Chemical Reviews* 119 (2019): 8781–8845.

7. Y. R. Luo, *Comprehensive Handbook of Chemical Bond Energies* (Boca Raton, FL: Taylor and Francis, 2007).

8. K. Kitaura and K. Morokuma, "A New Energy Decomposition Scheme for Molecular Interactions Within the Hartree-Fock Approximation," *International Journal of Quantum Chemistry* 10, no. 2 (1976): 325–340.

9. Y. Mo, J. Gao, and S. D. Peyerimhoff, "Energy Decomposition Analysis of Intermolecular Interactions Using a Block-Localized Wave Function Approach," *Journal of Chemical Physics* 112, no. 13 (2000): 5530–5538.

10. D. S. Levine and M. Head-Gordon, "Energy Decomposition Analysis of Single Bonds Within Kohn-Sham Density Functional Theory," *PNAS* 114, no. 48 (2017): 12649–12656.

11. L. Zhao, M. Hermann, W. H. E. Schwarz, and G. Frenking, "The Lewis electron-Pair Bonding Model: Modern Energy Decomposition Analysis," *Nature Reviews Chemistry* 3 (2019): 49–62.

12. J. Andrés, P. W. Ayers, R. A. Boto, et al., "Nine questions on energy decomposition analysis," *Journal of Computational Chemistry* 40 (2019): 2248–2283.

13. F. M. Bickelhaupt and K. N. Houk, "Analyzing Reaction Rates With the Distortion/Interaction-Activation Strain Model," *Angewandte Chemie, International Edition* 56, no. 34 (2017): 10070–10086.

14. D. Cremer and E. Kraka, "From Molecular Vibrations to Bonding, Chemical Reactions, and Reaction Mechanism," *Current Organic Chemistry* 14 (2010): 1524–1560.

15. R. Kalescky, E. Kraka, and D. Cremer, "Are Carbon-Halogen Double and Triple Bonds Possible?," *International Journal of Quantum Chemistry* 114 (2014): 1060–1072.

16. R. Kalescky, W. Zou, E. Kraka, and D. Cremer, "Quantitative Assessment of the Multiplicity of Carbon-Halogen Bonds: Carbenium and Halonium Ions With F, Cl, Br, and I," *Journal of Physical Chemistry. A* 118 (2014): 1948–1963.

17. V. Oliveira, E. Kraka, and D. Cremer, "Quantitative Assessment of Halogen Bonding Utilizing Vibrational Spectroscopy," *Inorganic Chemistry* 56 (2016): 488–502.

18. D. Setiawan, D. Sethio, D. Cremer, and E. Kraka, "From Strong to Weak NF Bonds: On the Design of a New Class of Fluorinating Agents," *Physical Chemistry Chemical Physics* 20 (2018): 23913–23927.

19. D. Sethio, V. Oliveira, and E. Kraka, "Quantitative Assessment of Tetrel Bonding Utilizing Vibrational Spectroscopy," *Molecules* 23 (2018): 2763.

20. R. F. W. Bader, "A Quantum Theory of Molecular Structure and Its Applications," *Chemical Reviews* 91, no. 5 (1991): 893–928.

21. R. F. W. Bader, *Atoms in Molecules: A Quantum Theory (International Series of Monographs on Chemistry)* (Oxford, UK: Clarendon Press, 1994).

22. P. L. Popelier, *Atoms in Molecules: An Introduction* (England: Prentice Hall, 2000).

23. R. F. W. Bader, "A Bond Path: A Universal Indicator of Bonded Interactions," *Journal of Physical Chemistry. A* 102, no. 37 (1998): 7314–7323.

24. A. Savin, R. Nesper, S. Wengert, and T. F. Fässler, "ELF: The Electron Localization Function," *Angewandte Chemie* 36, no. 17 (1997): 1808–1832.

25. P. J. Robinson and A. N. Alexandrova, "Assessing the Bonding Properties of Individual Molecular Orbitals," *Journal of Physical Chemistry. A* 119 (2015): 12862–12867.

26. F. Weinhold, C. R. Landis, and E. D. Glendening, "What Is NBO Analysis and How Is It Useful?," *International Reviews in Physical Chemistry* 35, no. 3 (2016): 399–440.

27. J. J. P. Stewart, "An Examination of the Nature of Localized Molecular Orbitals and Their Value in Understanding Various Phenomena That Occur in Organic Chemistry," *Journal of Molecular Modeling* 25, no. 1 (2018): 7.

28. E. Kraka, M. Quintano, H. W. La Force, J. J. Antonio, and M. Freindorf, "The Local Vibrational Mode Theory and Its Place in the Vibrational Spectroscopy Arena," *Journal of Physical Chemistry. A* 126 (2022): 8781–8798.

29. E. Kraka, W. Zou, and Y. Tao, "Decoding Chemical Information From Vibrational Spectroscopy Data: Local Vibrational Mode Theory," *WIREs Computational Molecular Science* 10 (2020): 1480.

30. R. T. Moura, Jr., M. Quintano, C. V. Santos-Jr, et al., "Featuring a New Computational Protocol for the Estimation of Intensity and Overall Quantum Yield in Lanthanide Chelates With Applications to Eu(III) Mercapto-Triazole Schiff Base Ligands," *Optical Materials: X* 16 (2022): 100216.

31. R. T. Moura, Jr., M. Quintano, J. J. Antonio, M. Freindorf, and E. Kraka, "Automatic Generation of Local Vibrational Mode Parameters: From Small to Large Molecules and QM/MM Systems," *Journal of Physical Chemistry. A* 126 (2022): 9313–9331.

32. M. Quintano, R. T. Moura, Jr., and E. Kraka, "The pK_a Rule in Light of Local Mode Force Constants," *Chemical Physics Letters* 826 (2023): 140654.

33. F. Bodo, A. Erba, E. Kraka, and R. T. Moura, Jr., "Chemical bonding in Uranium-based materials: A local vibrational mode case study of $Cs_2UO_2Cl_4$ and UCl_4 crystals," *Journal of Computational Chemistry* 45, no. 14 (2024): 1130–1142.

34. M. Quintano, R. T. Moura, Jr., and E. Kraka, "Exploring Jahn-Teller Distortions: A Local Vibrational Mode Perspective," *Journal of Molecular Modeling* 30, no. 4 (2024): 102.

35. R. T. Moura, Jr., A. N. C. Neto, O. L. Malta, and R. L. Longo, "Overlap Properties of Chemical Bonds in Generic Systems Including Unusual Bonding Situations," *Journal of Molecular Modeling* 26, no. 11 (2020): 301.

36. O. L. Malta, H. J. Batista, and L. D. Carlos, "Overlap Polarizability of a Chemical Bond: A Scale of Covalency and Application to Lanthanide Compounds," *Chemical Physics* 282, no. 1 (2002): 21–30.

37. C. V. Santos, S. A. Monteiro, A. S. C. Soares, I. C. A. Souto, and R. T. Moura, Jr., "Decoding Chemical Bonds: Assessment of the Basis Set Effect on Overlap Electron Density Descriptors and Topological Properties in Comparison to QTAIM," *Journal of Physical Chemistry. A* 127, no. 38 (2023): 7997–8014.

38. L. D. Carlos, O. L. Malta, and R. Q. Albuquerque, "A Covalent Fraction Model for Lanthanide Compounds," *Chemical Physics Letters* 415, no. 4–6 (2005): 238–242.

39. O. L. Malta, R. T. Moura, Jr., and R. L. Longo, "Electron Energy-Loss Cross Sections for the Chemical Bond Overlap Plasmon of the Hydrogen Molecule," *Journal of the Brazilian Chemical Society* 21, no. 3 (2010): 476–480.

40. R. T. Moura, Jr., G. C. S. Duarte, T. E. da Silva, O. L. Malta, and R. L. Longo, "Features of Chemical Bonds Based on the Overlap Polarizabilities: Diatomic and Solid-State Systems With the Frozen-Density Embedding Approach," *Physical Chemistry Chemical Physics* 17 (2015): 7731–7742.

41. C. V. Santos-Jr, M. A. F. de Souza, E. Kraka, and R. T. Moura, Jr., "Analysis of Spectator Chemical Bonds in SN2@C and @Si Reaction Mechanisms in the Gas Phase," *Chemical Physics Letters* 787 (2022): 139282.

42. R. T. Moura, Jr., A. N. C. Neto, R. L. Longo, and O. L. Malta, "On the Calculation and Interpretation of Covalency in the Intensity Parameters of 4f—4f Transitions in Eu^{3+} Complexes Based on the Chemical Bond Overlap Polarizability," *Journal of Luminescence* 170 (2016): 420–430.

43. A. N. C. Neto, R. T. Moura, Jr., E. C. Aguiar, C. V. Santos, and M. A. F. L. B. de Medeiros, "Theoretical Study of Geometric and Spectroscopic

Properties of Eu(III) Complexes With Ruhemann's Purple Ligands," *Journal of Luminescence* 201 (2018): 451–459.

44. A. N. Carneiro Neto and R. T. Moura, Jr., "Overlap Integrals and Excitation Energies Calculations in Trivalent Lanthanides 4f Orbitals in Pairs Ln-L (L = Ln, N, O, F, P, S, Cl, Se, Br, and I)," *Chemical Physics Letters* 757 (2020): 137884.

45. C. V. Santos-Jr, G. M. B. Da Silva, R. P. Dias, R. T. Moura, Jr., and J. C. S. Da Silva, "Exploring Trans Effect Concept in Pt(II) Complexes Through the Quantum Theory of Atoms in Molecules and Chemical Bond Overlap Model Perspectives," *Advanced Theory and Simulations* 7, no. 5 (2024): 2301148.

46. R. T. Moura, Jr., O. L. Malta, and R. L. Longo, "The Chemical Bond Overlap Plasmon as a Tool for Quantifying Covalency in Solid State Materials and Its Applications to Spectroscopy," *International Journal of Quantum Chemistry* 111, no. 7–8 (2011): 1626–1638.

47. R. T. Moura, Jr., J. A. Oliveira, I. A. Santos, et al., "Theoretical Evidence of the Singlet Predominance in the Intramolecular Energy Transfer in Ruhemann's Purple Tb(III) Complexes," *Advanced Theory and Simulations* 4, no. 3 (2021): 2000304.

48. R. T. Moura, Jr., A. N. C. Neto, E. C. Aguiar, et al., "(Invited) JOYSpectra: A Web Platform for Luminescence of Lanthanides," *Optical Materials: X* 11 (2021): 100080.

49. A. D. Becke, "Perspective: Fifty Years of Density-Functional Theory in Chemical Physics," *Journal of Chemical Physics* 140, no. 18 (2014): 18A301.

50. B. O. Roos, *The Complete Active Space Self-Consistent Field Method and Its Applications in Electronic Structure Calculations* (Chichester, England: John Wiley & Sons, Ltd, 1987), 399–445.

51. K. Andersson, P. A. Malmqvist, B. O. Roos, A. J. Sadlej, and K. Wolinski, "Second-Order Perturbation Theory With a CASSCF Reference Function," *Journal of Chemical Physics* 94, no. 14 (1990): 5483–5488.

52. K. Andersson, P. Å. Malmqvist, and B. O. Roos, "Second-Order Perturbation Theory With a Complete Active Space Self-Consistent Field Reference Function," *Journal of Chemical Physics* 96, no. 2 (1992): 1218–1226.

53. C. Angeli, R. Cimiraglia, S. Evangelisti, T. Leininger, and J. P. Malrieu, "Introduction of n-electron Valence States for Multireference Perturbation Theory," *Journal of Chemical Physics* 114, no. 23 (2001): 10252–10264.

54. E. Kraka, Y. He, and D. Cremer, "Quantum Chemical Descriptions of FOOF: The Unsolved Problem of Predicting Its Equilibrium Geometry," *Journal of Physical Chemistry. A* 105 (2001): 3269–3276.

55. J. J. Wardzala, D. S. King, L. Ogunfowora, B. Savoie, and L. Gagliardi, "Organic Reactivity Made Easy and Accurate With Automated Multireference Calculations," *ACS Central Science* 10, no. 4 (2024): 833–841.

56. A. L. Wysocki and K. Park, "Relativistic Douglas–Kroll–Hess Calculations of Hyperfine Interactions Within First-Principles Multireference Methods," *Journal of Chemical Physics* 160, no. 22 (2024): 224102.

57. A. Loreti, V. M. Freixas, D. Avagliano, et al., "WFOT: A Wave Function Overlap Tool Between Single- and Multi-Reference Electronic Structure Methods for Spectroscopy Simulation," *Journal of Chemical Theory and Computation* 20, no. 11 (2024): 4804–4819.

58. P. Verma and D. G. Truhlar, "Can Kohn–Sham Density Functional Theory Predict Accurate Charge Distributions for Both Single-Reference and Multi-Reference Molecules?," *Physical Chemistry Chemical Physics* 19, no. 20 (2017): 12898–12912.

59. G. Li Manni, R. K. Carlson, S. Luo, et al., "Multiconfiguration Pair-Density Functional Theory," *Journal of Chemical Theory and Computation* 10, no. 9 (2014): 3669–3680.

60. R. K. Carlson, D. G. Truhlar, and L. Gagliardi, "Multiconfiguration Pair-Density Functional Theory: A Fully Translated Gradient Approximation and Its Performance for Transition Metal Dimers and the Spectroscopy of Re_2Cl_{82}," *Journal of Chemical Theory and Computation* 11, no. 9 (2015): 4077–4085.

61. S. Grimme and M. Waletzke, "Multi-Reference Møller–Plesset Theory: Computational Strategies for Large Molecules," *Physical Chemistry Chemical Physics* 2, no. 10 (2000): 2075–2081.

62. R. McWeeny and B. T. Sutcliffe, "Methods of Molecular Quantum Mechanics," in *Pure and Applied Mathematics* (New York: Academic Press, 1969).

63. M. Malček, B. Vénosová, I. Puškárová, J. Kožíšek, M. Gall, and L. Bučinský, "Coordination Bonding in Dicopper and Dichromium Tetrakis(μ-Acetato)-diaqua Complexes: Nature, Strength, Length, and Topology," *Journal of Computational Chemistry* 41, no. 7 (2019): 698–714.

64. G. Li, L. Meng, H. Zhang, X. Li, and Y. Zeng, "Electronic Structure of Triangular M_3 (M = B, Al, Ga): Nonclassical Three-Center Two electron π Bond and σ Delocalization," *Physical Chemistry Chemical Physics* 22, no. 32 (2020): 18071–18077.

65. N. I. Giricheva, V. V. Sliznev, A. S. Alikhanyan, E. A. Morozova, and G. V. Girichev, "Molecular Structure of Gaseous Oxopivalate Co(II): Electronic States of Various Multiplicities," *International Journal of Molecular Sciences* 24, no. 17 (2023): 13224.

66. C. G. Pech, P. A. B. Haase, D. C. Sergentu, et al., "Quantum Chemical Topology at the Spin–Orbit Configuration Interaction Level: Application to Astatine Compounds," *Journal of Computational Chemistry* 41, no. 23 (2020): 2055–2065.

67. L. Reuter and A. Lüchow, "On the Connection Between Probability Density Analysis, QTAIM, and VB Theory," *Physical Chemistry Chemical Physics* 22, no. 44 (2020): 25892–25903.

68. Y. A. Zhabanov, V. V. Sliznev, I. V. Ryzhov, and P. A. Stuzhin, "Peculiarities of Electronic Structure and Chemical Bonding in iron and Cobalt Metal Complexes of Porphyrazine and Tetra(1, 2, 5-Thiadiazole) porphyrazine," *Journal of Porphyrins and Phthalocyanines* 24, no. 9 (2020): 1146–1154.

69. H. Lischka, R. Shepard, R. M. Pitzer, et al., "High-Level Multireference Methods in the Quantum-Chemistry Program System COLUMBUS: Analytic MR-CISD and MR-AQCC Gradients and MR-AQCC-LRT for Excited States, GUGA Spin–Orbit CI and Parallel CI Density," *Physical Chemistry Chemical Physics* 3, no. 5 (2001): 664–673.

70. H. Lischka, T. Müller, P. G. Szalay, I. Shavitt, R. M. Pitzer, and R. Shepard, "Columbus—A Program System for Advanced Multireference Theory Calculations," *Wiley Interdisciplinary Reviews: Computational Molecular Science* 1, no. 2 (2011): 191–199.

71. R. Shepard, H. Lischka, P. G. Szalay, T. Kovar, and M. Ernzerhof, "A General Multireference Configuration Interaction Gradient Program," *Journal of Chemical Physics* 96, no. 3 (1992): 2085–2098.

72. H. Lischka, M. Dallos, and R. Shepard, "Analytic MRCI Gradient for Excited States: Formalism and Application to the n-pi Valence- and n-(3s, 3p) Rydberg States of Formaldehyde," *Molecular Physics* 100, no. 11 (2002): 1647–1658.

73. P. G. Szalay, T. Müller, G. Gidofalvi, H. Lischka, and R. Shepard, "Multiconfiguration Self-Consistent Field and Multireference Configuration Interaction Methods and Applications," *Chemical Reviews* 112, no. 1 (2011): 108–181.

74. R. Di Felice, M. L. Mayes, R. M. Richard, et al., "A Perspective on Sustainable Computational Chemistry Software Development and Integration," *Journal of Chemical Theory and Computation* 19, no. 20 (2023): 7056–7076.

75. F. Plasser and H. Lischka, "Analysis of Excitonic and Charge Transfer Interactions From Quantum Chemical Calculations," *Journal of Chemical Theory and Computation* 8, no. 8 (2012): 2777–2789.

76. M. Barbatti, M. Ruckenbauer, F. Plasser, et al., "Newton-X: A Surface-Hopping Program for Nonadiabatic Molecular Dynamics," *WIREs Computational Molecular Science* 4, no. 1 (2013): 26–33.

77. H. Lischka, D. Nachtigallová, A. J. A. Aquino, et al., "Multireference Approaches for Excited States of Molecules," *Chemical Reviews* 118, no. 15 (2018): 7293–7361.

78. S. Pathak, L. Lang, and F. Neese, "A Dynamic Correlation Dressed Complete Active Space Method: Theory, Implementation, and Preliminary Applications," *Journal of Chemical Physics* 147, no. 23 (2017): 234109.

79. M. Fugel, J. Beckmann, D. Jayatilaka, G. V. Gibbs, and S. Grabowsky, "A Variety of Bond Analysis Methods, One Answer? An Investigation of the Element-Oxygen Bond of Hydroxides H_nXOH," *European Journal of Chemistry* 24, no. 23 (2018): 6248–6261.

80. J. Pipek and P. G. Mezey, "A Fast Intrinsic Localization Procedure Applicable for Ab-Initio and Semi-Empirical Linear Combination of Atomic Orbital Wave Functions," *Journal of Chemical Physics* 90, no. 9 (1989): 4916–4926.

81. S. Lehtola and H. Jónsson, "Pipek-Mezey Orbital Localization Using Various Partial Charge Estimates," *Journal of Chemical Theory and Computation* 10, no. 2 (2014): 642–649.

82. T. Helgaker, P. Jørgensen, and J. Olsen, "Spin in Second Quantization," in *Molecular Electronic-Structure Theory* (New York: John Wiley & Sons, Ltd, 2000), 34–79.

83. X. Fradera, M. A. Austen, and R. F. W. Bader, "The Lewis Model and Beyond," *Journal of Physical Chemistry A* 103, no. 2 (1999): 304–314.

84. J. C. Slater, "The Theory of Complex Spectra," *Physics Review* 34 (1929): 1293–1322.

85. E. U. Condon, "The Theory of Complex Spectra," *Physics Review* 36 (1930): 1121–1133.

86. C. V. Santos-Jr, E. M. Lima, and R. T. Moura, Jr., "Numerical Integration of Overlap electron Densities: Parallelization Strategies for a Good Load Balancing Using OpenMP," *Computational and Theoretical Chemistry* 1206 (2021): 113457.

87. M. J. Frisch, G. W. Trucks, H. B. Schlegel, et al., "Gaussian 09 Revision A.2," (2009).

88. F. Neese, "The ORCA Program System," *Wiley Interdisciplinary Reviews: Computational Molecular Science* 2, no. 1 (2011): 73–78.

89. T. Zhu, P. de Silva, and T. V. Voorhis, "Self-Attractive Hartree Decomposition: Partitioning Electron Density Into Smooth Localized Fragments," *Journal of Chemical Theory and Computation* 14, no. 1 (2017): 92–103.

90. T. Zhu, P. de Silva, and T. V. Voorhis, "Implementation of the Many-Pair Expansion for Systematically Improving Density Functional Calculations of Molecules," *Journal of Chemical Theory and Computation* 15, no. 2 (2019): 1089–1101.

91. D. S. Levine and M. Head-Gordon, "Clarifying the Quantum Mechanical Origin of the Covalent Chemical Bond," *Nature Communications* 11, no. 1 (2020): 4893.

92. Á. Martín Pendás and E. Francisco, "The Role of References and the Elusive Nature of the Chemical Bond," *Nature Communications* 13, no. 1 (2022): 3327.

93. D. Cremer and E. Kraka, "Chemical Bonds Without Bonding Electron Density? Does the Difference Electron-Density Analysis Suffice for a Description of the Chemical Bond?," *Angewandte Chemie* 23, no. 8 (1984): 627–628.

94. D. Cremer and E. Kraka, "A Description of the Chemical Bond in Terms of Local Properties of Electron Density and Energy," *Croatica Chemica Acta* 57 (1984): 1259–1281.

95. V. P. Oliveira, E. Kraka, and F. B. C. Machado, "Pushing 3c–4e Bonds to the Limit: A Coupled Cluster Study of Stepwise Fluorination of First-Row Atoms," *Inorganic Chemistry* 58, no. 21 (2019): 14777–14789.

96. A. H. Pakiari and K. Eskandari, "Closed Shell Oxygen–Oxygen Bonding Interaction Based on Electron Density Analysis," *Journal of Molecular Structure* 806, no. 1–3 (2007): 1–7.

97. I. Love, "Polar Covalent Bonds: An AIM Analysis of S, O Bonds," *Journal of Physical Chemistry* 113, no. 11 (2009): 2640–2646.

98. P. Farfán, S. Gómez, and A. Restrepo, "Dissection of the Mechanism of the Wittig Reaction," *Journal of Organic Chemistry* 84, no. 22 (2019): 14644–14658.

99. E. B. Wilson, J. C. Decius, and P. C. M. Cross, *Molecular Vibrations. The Theory of Infrared and Raman Vibrational Spectra* (New York: McGraw-Hill, 1955).

100. E. B. Wilson, "Some Mathematical Methods for the Study of Molecular Vibrations," *Journal of Chemical Physics* 9 (1941): 76–84.

101. Z. Konkoli and D. Cremer, "A New Way of Analyzing Vibrational Spectra. I. Derivation of Adiabatic Internal Modes," *International Journal of Quantum Chemistry* 67 (1998): 1–9.

102. Z. Konkoli, J. A. Larsson, and D. Cremer, "A New Way of Analyzing Vibrational Spectra. II. Comparison of Internal Mode Frequencies," *International Journal of Quantum Chemistry* 67 (1998): 11–27.

103. V. Barone, S. Alessandrini, M. Biczysko, et al., "Computational Molecular Spectroscopy," *Nature Reviews Methods Primers* 1, no. 1 (2021): 38.

104. C. Riplinger, P. Pinski, U. Becker, E. F. Valeev, and F. Neese, "Sparse Maps—A Systematic Infrastructure for Reduced-Scaling Electronic Structure Methods. II. Linear Scaling Domain Based Pair Natural Orbital Coupled Cluster Theory," *Journal of Chemical Physics* 144, no. 2 (2016): 024109.

105. C. Riplinger and F. Neese, "An Efficient and Near Linear Scaling Pair Natural Orbital Based Local Coupled Cluster Method," *Journal of Chemical Physics* 138, no. 3 (2013): 034106.

106. C. Riplinger, B. Sandhoefer, A. Hansen, and F. Neese, "Natural Triple Excitations in Local Coupled Cluster Calculations With Pair Natural Orbitals," *Journal of Chemical Physics* 139, no. 13 (2013): 134101.

107. D. Rappoport and F. Furche, "Property-Optimized Gaussian Basis Sets for Molecular Response Calculations," *Journal of Chemical Physics* 133, no. 13 (2010): 134105.

108. F. Weigend, F. Furche, and R. Ahlrichs, "Gaussian Basis Sets of Quadruple Zeta Valence Quality for Atoms H–Kr," *Journal of Chemical Physics* 119, no. 24 (2003): 12753–12762.

109. F. Weigend, A. Köhn, and C. Hättig, "Efficient Use of the Correlation Consistent Basis Sets in Resolution of the Identity MP2 Calculations," *Journal of Computational Chemistry* 116, no. 8 (2002): 3175–3183.

110. M. S. Gordon, M. W. Schmidt, G. M. Chaban, K. R. Glaesemann, W. J. Stevens, and C. Gonzalez, "A Natural Orbital Diagnostic for Multiconfigurational Character in Correlated Wave Functions," *Journal of Chemical Physics* 110, no. 9 (1999): 4199–4207.

111. W. Zou, D. Nori-Shargh, and J. E. Boggs, "On the Covalent Character of Rare Gas Bonding Interactions: A New Kind of Weak Interaction," *Journal of Physical Chemistry. A* 117, no. 1 (2012): 207–212.

112. T. Lu and F. Chen, "Multiwfn: A Multifunctional Wavefunction Analyzer," *Journal of Computational Chemistry* 33, no. 5 (2011): 580–592.

113. W. Zou, R. Moura, Jr., M. Quintano, et al., *Computational and Theoretical Chemistry Group (CATCO)* (Dallas, TX, USA: Southern Methodist University, 2024).

114. E. F. Pettersen, T. D. Goddard, C. C. Huang, et al., "UCSF ChimeraX: Structure Visualization for Researchers, Educators, and Developers," *Protein Science* 30, no. 1 (2021): 70–82.

115. T. D. Goddard, C. C. Huang, E. C. Meng, et al., "UCSF ChimeraX: Meeting Modern Challenges in Visualization and Analysis," *Protein Science* 27 (2018): 14–25.

116. A. J. Schaefer, V. M. Ingman, and S. E. Wheeler, "SEQCROW: A ChimeraX Bundle to Facilitate Quantum Chemical Applications to Complex Molecular Systems," *Journal of Computational Chemistry* 42, no. 24 (2021): 1750–1754.

117. V. M. Ingman, A. J. Schaefer, L. R. Andreola, and S. E. Wheeler, "QChASM: Quantum Chemistry Automation and Structure Manipulation," *WIREs Computational Molecular Science* 11, no. 4 (2021): e1510.

118. S. Klein, E. Kochanski, A. Strich, and A. J. Sadlej, "Electric Properties of the Water Molecule in 1A1, 1B1, and 3B1 Electronic States: Refined CASSCF and CASPT2 Calculations," *Theoretica Chimica Acta* 94, no. 2 (1996): 75–91.

119. R. D. Johnson, III, *NIST Computational Chemistry Comparison and Benchmark Database NIST Standard Reference Database* Number 101, accessed 21, May 2023. (National Institute of Standards and Technology, 2022), http://cccbdb.nist.gov/.

120. C. V. Santos-Jr, E. C. Aguiar, A. N. Carneiro Neto, and R. T. Moura, Jr., "Adaptive Guided Stochastic Optimization: A Novel Approach for Fitting the Theoretical Intensity Parameters for Lanthanide Compounds," *Optical Materials: X* 20 (2023): 100275.

121. W. G. Barbosa, C. V. Santos-Jr, R. B. Andrade, J. R. Lucena, Jr., and R. T. Moura, Jr., "Bond Analysis in Meta- and Para-Substituted Thiophenols: Overlap Descriptors, Local Mode Analysis, and QTAIM," *Journal of Molecular Modeling* 30, no. 5 (2024): 139.

122. S. Shaik, D. Danovich, B. Silvi, D. L. Lauvergnat, and P. C. Hiberty, "Charge-Shift Bonding—A Class of Electron-Pair Bonds That Emerges From Valence Bond Theory and Is Supported by the Electron Localization Function Approach," *Chemistry – A European Journal* 11, no. 21 (2005): 6358–6371.

123. T. Nottoli, J. Gauss, and F. Lipparini, "Second-Order CASSCF Algorithm With the Cholesky Decomposition of the Two-Electron Integrals," *Journal of Chemical Theory and Computation* 17, no. 11 (2021): 6819–6831.

124. H. A. Bent, "An Appraisal of Valence-Bond Structures and Hybridization in Compounds of the First-Row Elements," *Chemical Reviews* 61, no. 3 (1961): 275–311.

125. I. V. Alabugin, S. Bresch, and M. Manoharan, "Hybridization Trends for Main Group Elements and Expanding the Bent's Rule Beyond Carbon: More Than Electronegativity," *Journal of Physical Chemistry. A* 118, no. 20 (2014): 3663–3677.

126. A. J. Bridgeman and J. Rothery, "Bonding in Mixed Halogen and Hydrogen Peroxides," *Journal of the Chemical Society, Dalton Transactions* (1999): 4077–4082.

127. K. Sivalingam, M. Krupicka, A. A. Auer, and F. Neese, "Comparison of Fully Internally and Strongly Contracted Multireference Configuration Interaction Procedures," *Journal of Chemical Physics* 145, no. 5 (2016): 054104.

128. J. Bauschlicher, W. Charles, and S. R. Langhoff, "Full Configuration-Interaction Study of the Ionic–Neutral Curve Crossing in LiF," *Journal of Chemical Physics* 89, no. 7 (1988): 4246–4254.

Supporting Information

Additional supporting information can be found online in the Supporting Information section.